



Research Paper

Megahertz emission of massive early-type stars in the Cygnus region

P. Benaglia^{1,2} , M. De Becker³, C. H. Ishwara-Chandra⁴, H. T. Intema^{5,6}  and N. L. Isequilla²

¹Instituto Argentino de Radioastronomía, CONICET & CICPBA, CC5 (1897) Villa Elisa, Prov. de Buenos Aires, Argentina, ²Facultad de Ciencias Astronómicas y Geofísicas, UNLP, Paseo del Bosque s/n, (1900) La Plata, Argentina, ³Space sciences, Technologies and Astrophysics Research (STAR) Institute, University of Liège, Quartier Agora, 19c, Allée du 6 Août, B5c, B-4000 Sart Tilman, Belgium, ⁴National Centre for Radio Astrophysics (NCRA-TIFR), Pune 411 007, India, ⁵International Centre for Radio Astronomy Research, Curtin University, Bentley, WA 6102, Australia and ⁶Leiden Observatory, Leiden University, Niels Bohrweg 2, 2333 CA Leiden, the Netherlands

Abstract

Massive, early-type stars have been detected as radio sources for many decades. Their thermal winds radiate free-free continuum and in binary systems hosting a colliding-wind region, non-thermal emission has also been detected. To date, the most abundant data have been collected from frequencies higher than 1 GHz. We present here the results obtained from observations at 325 and 610 MHz, carried out with the Giant Metrewave Radio Telescope, of all known Wolf-Rayet and O-type stars encompassed in area of ~ 15 sq degrees centred on the Cygnus region. We report on the detection of 11 massive stars, including both Wolf-Rayet and O-type systems. The measured flux densities at decimeter wavelengths allowed us to study the radio spectrum of the binary systems and to propose a consistent interpretation in terms of physical processes affecting the wide-band radio emission from these objects. WR 140 was detected at 610 MHz, but not at 325 MHz, very likely because of the strong impact of free-free absorption (FFA). We also report—for the first time—on the detection of a colliding-wind binary system down to 150 MHz, pertaining to the system of WR 146, making use of complementary information extracted from the Tata Institute of Fundamental Research GMRT Sky Survey. Its spectral energy distribution clearly shows the turnover at a frequency of about 600 MHz, that we interpret to be due to FFA. Finally, we report on the identification of two additional particle-accelerating colliding-wind binaries, namely Cyg OB2 12 and ALS 15108 AB.

Keywords: radio continuum: stars – radiation mechanisms: non-thermal – stellar associations: individual: Cyg OB2

(Received 16 November 2019; revised 26 May 2020; accepted 1 June 2020)

1. Introduction

Massive, early-type stars—O, early B (OB), and Wolf-Rayet (WR) spectral type classes—are characterised by strong winds that deliver material and energy to their surroundings. Many of these stars are in binary or higher multiplicity systems. In such systems, stellar winds interact in a colliding-wind region (CWR), hence their designation as colliding-wind binaries or CWBs. Since the 70s, massive stars are known to be moderate sources of thermal radio emission, and in many cases, non-thermal (NT) radio emission has also been identified. The first is naturally explained as free-free radiation from the stellar winds (Wright & Barlow 1975). The NT contribution arises from synchrotron radiation produced by relativistic electrons in the presence of the local magnetic field in the CWR (e.g., Dougherty & Williams 2000). Consequently, NT radio emission constitutes a valuable tracer of particle acceleration in these systems. The mechanism responsible for the acceleration of relativistic electrons is very likely diffusive shock acceleration (Drury 1983; Eichler & Usov 1993). CWBs emit radio waves but are dim and scarce. Only the closer systems can be detected with current facilities, and intensity distribution maps could be obtained for a handful of them only (Benaglia et al.

2015; Sanchez-Bermudez et al. 2019, and references therein). As the NT emission arises from the CWR, a significant variability on the orbital time scale is expected and confirmed by adequate radio monitoring, such as in the case of the emblematic system WR 140 (White & Becker 1995). The most complete catalogue of particle-accelerating colliding-wind binaries (PACWBs) was published recently by De Becker & Raucq (2013) and contains around 40 objects and a complete compilation of properties of the objects along the entire electromagnetic spectrum.

On the one hand, only a limited fraction of massive early-type stars or systems have been observed in the 1- to 15-GHz frequency range, most of which with flux densities of the order of a few mJy. The brightest O-type PACWB is HD 167971 with a few tens of mJy (Blomme et al. 2007), and the absolute record for a PACWB so far is held by the recently discovered Apep system (WR+WR binary), with flux densities higher than 100 mJy (Callingham et al. 2019). On the other hand, observations at very low frequencies have been, up to now, very limited, due to instrumental constraints, mainly angular resolution but also sensitivity. The main antecedent to this work is that of Setia Gunawan et al. (2003). The authors scrutinised a $2^\circ \times 2^\circ$ area of Cygnus OB2 at 1.4 GHz and 350 MHz using the Westerbork Synthesis Radio Telescope (WSRT), to investigate hot massive stars. Their 350-MHz observations reached an angular resolution of about $55''$ and an average $1-\sigma$ flux density value of 2–3 mJy and resulted in the detection of three WR systems.

More recently, the Giant Metrewave Radio Telescope (GMRT) has proven its efficiency to study such stellar systems: Benaglia et al. (2019) reported on the study of WR 11 by means of

Author for correspondence: P. Benaglia, E-mail: pben.radio@gmail.com

Cite this article: Benaglia P, De Becker M, Ishwara-Chandra CH, Intema HT and Isequilla NL. (2020) Megahertz emission of massive early-type stars in the Cygnus region. *Publications of the Astronomical Society of Australia* 37, e030, 1–16. <https://doi.org/10.1017/pasa.2020.21>

© Astronomical Society of Australia 2020; published by Cambridge University Press

GMRT data from 150 MHz to 1.4 GHz, with detections at 325 and 610 MHz at angular resolutions ranging from 22 to 5". The synchrotron emission is stronger at lower frequencies, hence the relevance to consider GMRT observations to investigate the NT physics of these systems (De Becker, Ishwara-Chandra, & Benaglia 2019a). At frequencies lower than 1 GHz, turnover processes such as Razin–Tsytoich effect (RTE), FFA (thermal), and synchrotron self-absorption (SSA) may shape the spectrum depending on various factors that differ from one system to another. The characterisation of this turnover, that is, its nature and its occurrence frequency, constitutes to date a poorly investigated part in the description of the radio behaviour of massive star systems. It is clear that FFA is likely to be the dominant turnover process, because of the presence of the optically thick wind material. Characterising this FFA is important for a confrontation to hydro-radiative models of CWBs (including system orientation and geometry). However, if the spectrum inversion is due to RTE, the turnover frequency is related to the number density of thermal electrons and to the magnetic field strength in the emission region. SSA is less likely as it would require number densities in relativistic electrons certainly higher than expected in CWBs.

At the other end of the electromagnetic spectrum, significant progress has been made to model the emission from CWRs in massive binaries (see Del Palacio et al. 2016, and references therein). The high-energy NT photon emission has recently been modelled in three dimensions, taking into account particle acceleration and radiative losses leading to γ -ray emission (Reitberger et al. 2014a, 2014b; Reitberger et al. 2017). However, high-energy emission from PACWBs lies mainly below the detection thresholds of the current instrumentation. The only exceptions are η Car (Tavani et al. 2009; Abdo et al. 2010; Reitberger et al. 2015) and WR 11 (Pshirkov 2016; Martí-Devesa et al. 2020). For this reason, radio observations constitute the most adequate approach to investigate these systems, especially from the point of view of their NT physics.

We have carried out observations with the GMRT at two decimeter bands, on a region of ~ 15 sq deg, centred at RA,Dec(J2000) = 20:25:30, 42:00:00, that belongs to the Cygnus Rift, in the northern sky. We reached an angular resolution down to 10" and average rms down to 0.5 mJy per beam. These last numbers mean roughly an improvement in factor 5 both in angular resolution and sensitivity with respect to the previous survey of Cyg OB2 carried out with the WSRT. Some parts of this region were previously observed with the GMRT to investigate potential counterparts to TeV sources (Martí et al. 2007; Paredes et al. 2007), but this is the first time such a wide area of the Cygnus region is studied at sub-GHz frequencies with the mentioned settings. The region under study here is populated by plenty of WR and OB stars, including the archetypal systems WR 140, WR 146, WR 147, and Cyg X-3, and our project allowed us to measure the radio emission at their stellar positions. In Section 2, we briefly describe the observed region and its massive stellar content. Section 3 presents the observing details and data reduction. In Section 4, we show the results of the performed analysis. Our results are then discussed in Section 5, and we finally conclude in Section 6.

2. The region and sources under study

The sky area known as the Cygnus constellation ($-65^\circ \leq l \leq 95^\circ$, $-8^\circ \leq b \leq +8^\circ$) contains active star-forming regions relatively close by ($d \leq 2.5$ kpc). Despite that the high absorption in its line of sight prevents to accurately map the stellar population

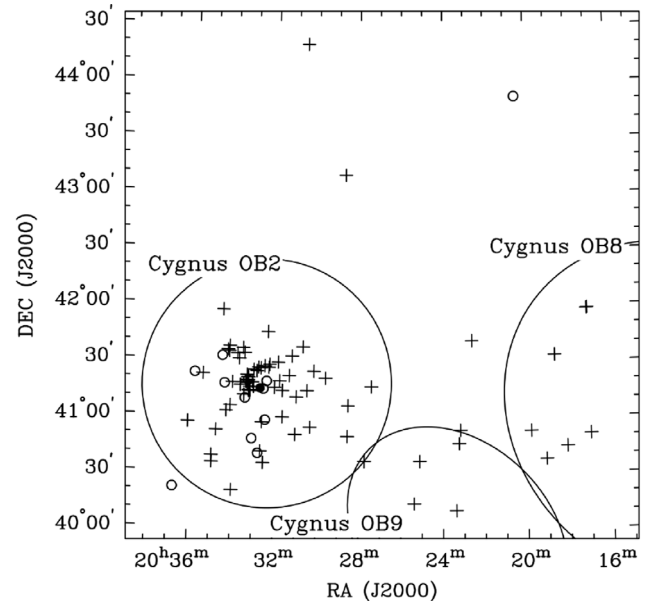


Figure 1. Observed area, showing the positions of the stars studied here, with open circles (detected cases) and crosses (undetected cases). The large ellipses mark the approximate extensions of the OB associations present in the area, according to Uyaniker et al. (2001).

at optical wavelengths, Cygnus stands as one of the richest and more crowded areas in the Galaxy regarding massive stellar objects (see the review paper by Reipurth & Schneider 2008). It houses nine OB associations together with bright open clusters (Uyaniker et al. 2001; Mahy et al. 2013). Among the stellar associations, Cyg OB2 is one of the youngest groups, with one hundred O stars and thousands of B stars (e.g., Knödseder 2000). At its side, Cyg OB8, and Cyg OB9 harbour about a hundred hot stars. We have carried out an investigation of the low-frequency emission at the position of the massive early-type stars belonging to the mentioned associations. Figure 1 presents the region surveyed here.

A first search for WR and O-type stars along the region portrayed in Fig. 1, using the SIMBAD astronomical database (<http://simbad.u-strasbg.fr/simbad/>), resulted in nine WR and around 90 O-type stars. The search was refined consulting the WR list at <http://www.pacrowther.staff.shef.ac.uk/WRcat/> (see also Rate & Crowther 2020) and the last version [GOSC v4.2] of the Galactic O-star catalogue (<https://gosc.cab.inta-csic.es/>) (see Maíz Apellániz et al. 2019, along with its references). The WR stars list is given in Table 1. The O-type stars considered here are listed in Table 2, and Table A.1 of Appendix A. Out of 87 O-type stars and systems, 50 of them are listed as GOSC members, while 28 appear in Comerón & Pasquali (2012).

3. GMRT observations and data reduction

The observations were collected along four campaigns (2013, 2014–2015, 2015, and 2016–2017) using the GMRT, at two bands, centred at 325 and 610 MHz, and cover a total sky area of about 15 square degrees. We used total intensity mode, with a bandwidth of 32 MHz and consisting of 256 spectral channels to minimise bandwidth smearing. As the common practice, we observed the flux density calibrators (3C286, 3C48, and 3C47) at the beginning and end of each run, and a phase calibrator 2052+365 for 5 min, bracketing the 30-min scans of the targeted FoVs. Five pointings were performed in the 325-MHz band and 47 in the 610-MHz

Table 1. WR stars in the observed field: measured radio flux density or upper limit, and spectral index information.

Name	Spectral type classification	RA, Dec _{J2000} (h,m,s),(d,'")	<i>d</i> (kpc)	<i>S</i> _{610MHz} (mJy)	Observing date(s)	<i>S</i> _{325MHz} (mJy)	Observing date(s)	α_{325}^{610}
WR 138a	WN8-9h ⁽¹⁾	20:17:08.12, +41:07:27.0	12.5 ⁽¹⁰⁾	<0.5	18/06/2015	<1.5	7/02,26/09/2015	–
WR 140	WC7pd+O5.5fc ⁽²⁾	20:20:27.98, +43:51:16.3	1.64 ⁽¹⁰⁾	0.87 ± 0.10	17/07/2016	<0.5	6/02/2015	> 0.8
WR 142a	WC8 ⁽³⁾	20:24:06.19, +41:25:33.8	1.81 ⁽¹⁰⁾	<1.0	17/08/2015	<1.75	26/10/2014	–
WR 142b	WN6 ⁽⁴⁾	20:28:14.56, +43:39:25.5	1.77 ⁽¹⁰⁾	<0.75	1/07/2016	<1.25	6/02/2015	–
WR 144	WC4 ⁽⁵⁾	20:32:03.02, +41:15:20.5	1.75 ⁽¹⁰⁾	<0.75	14/07,8/08/2016	<1.25	4/11/2013	–
WR 145	WN7o/CE+O7V((f)) ⁽⁶⁾	20:32:06.28, +40:48:29.5	1.46 ⁽¹⁰⁾	<0.75	29/11/2014	<1.5	4/11/2013	–
WR 145a	WN4-6+CO ⁽⁷⁾	20:32:25.78, +40:57:27.9	7.4	66 ± 0.5	29/11/2014,14/07,8/08/2016	27 ± 0.5	4/11/2013	1.42 ± 0.07
WR 146	WC6e+O8I-III ⁽⁸⁾	20:35:47.09, +41:22:44.7	1.1 ⁽¹⁰⁾	121 ± 4	29/11/2014	111 ± 2	4/11/2013	0.1 ± 0.04
WR 147	WN8(h)+B0.5V ⁽⁹⁾	20:36:43.60, +40:21:08.0	1.79 ⁽¹⁰⁾	20.6 ± 0.3	11,21/08/2016	<20	4/11/2013	> 0

References: (1) Gvarnadamze et al. (2009); (2) Fahed et al. (2011); (3) Pasquali et al. (2002); (4) Littlefield et al. (2012); (5) Sander, Hamann, & Todt (2012); (6) Muntean et al. (2009); (7) Koljonen & Maccarone (2017); (8) Lépine et al. (2001); (9) Williams et al. (1997); (10) Rate & Crowther (2020). RA, Dec (J2000): optical positions.

Table 2. Measured radio flux density or upper limit, and spectral index information of the detected O-type stars in the observed field.

Name	Spectral type classification	RA _{J2000} (h,m,s)	Dec _{J2000} (d,'")	<i>S</i> _{610MHz} (mJy)	Observing date(s)	<i>S</i> _{325MHz} (mJy)	Observing date(s)	α_{325}^{610}
Cyg OB2-5	(O6.5:Iaf+e + O7Iaf+e) + OB + O7 Ib(f)p var? ⁽¹⁾⁽²⁾	20 32 22.42	+41 18 19.0	4.0 ± 0.15	14/07,8/08/2016	5.5 ± 0.3	4/11/2013	−0.52 ± 0.27
Cyg OB2-A11	O7Ib(f) ⁽³⁾	20 32 31.54	+41 14 08.21	0.5 ± 0.1	14/07,8/08/2016	<1.5	4/11/2013	> −1.9
ALS 19624	O8II((f)) ⁽⁴⁾	20 33 02.92	+40 47 25.3	0.5 ± 0.1	29/11/2014	<1.5	4/11/2013	> −1.6
Cyg OB2-8A	O6Ib(fc) + O4.5:III:(fc) ⁽³⁾	20 33 15.08	+41 18 50.51	2.4 ± 0.2	14/07,8/08/2016	<2.3	4/11/2013	> 0.1
ALS 15108 AB	O6IV((f)) ⁽³⁾ + companion?	20 33 23.46	+41 09 13.0	0.95 ± 0.2	14/07,8/08/2016	1.25 ± 0.2	4/11/2013	−0.44 ± 0.96
Cyg OB2-73	O8Vz + O8Vz ⁽³⁾	20 34 21.93	+41 17 01.7	0.4 ± 0.1	14/07,8/08/2016	<2	4/11/2013	> −2.5
Cyg OB2-335	O7V((f)) + O7IV((f)) ⁽⁵⁾	20 34 29.60	+41 31 45.5	5.4 ± 0.2	29/11/2014	2.6 ± 0.3	4/11/2013	1.16 ± 0.44

References for spectral-type classification: (1) Maiz Apellániz et al. (2019); (2) Kennedy et al. (2010); (3) Maiz Apellániz et al. (2016); (4) Comerón & Pasquali (2012); (5) GOSC v4.2 (<https://gosc.cab.inta-csic.es/>). RA, Dec (J2000): optical positions.

band. The total observing time was 172 h which were divided so as to achieve near uniform noise in the survey. The fields of view of Giant Metrewave Radio Telescope are $81' \pm 4'$ and $43' \pm 3'$ at 325 and 610 MHz, respectively.^a Additional details in the observing process, like FoV centres, exact dates of observation, and name of calibrators used are given in Benaglia et al. (2020).

The data were reduced by means of the Source Peeling and Atmospheric Modeling (SPAM) routines (Intema 2014). The SPAM pipeline allowed calibration and flagging of each FoV. It also accounted for the T_{sys} correction for excess background towards the science target. For the 325-MHz FoVs, the correction factor ranged from 1.7 to 3.6, and for 610 MHz, from 1.22 to 1.75, the larger values near the galactic plane. The process included several rounds of self-calibration to the antenna phases. The images were primary beam corrected and finally combined in a mosaic, weighting them with the inverse of the variance.

The images were built with robust weighting of -1 , since we were more interested in discrete sources. Thus extended emission could not be imaged at its best. The used settings combined with the complex diffuse structure in the Cygnus region yielded to variations in the rms across the images. The average rms attained in the final mosaics is 0.5 mJy per beam at 325 MHz and 0.2 mJy per beam at 610 MHz. The synthesised beams were set to $10'' \times 10''$ and $6'' \times 6''$.

^aGMRT Observer's Manual; https://www.ncra.tifr.res.in/ncra/gmrt/gmrt-users/observing-help/manual_7jul15.pdf.

4. Results

We looked for radio emission at the location of the WR and O-type stars in the observed region. We claimed a detection if the optical position of the star/system is located within the radio emission loci (i.e., the size of the synthesised beam for discrete radio sources), and if the radio flux density remained above three times the rms of the surrounding area. We list the detection results on the WR stars in Table 1, including upper limits (3rms) of the flux density for the undetected cases. The flux densities related to the detected O-type stars are given in Table 2. The detected radio sources at the positions of WR and O-type stars are presented in Figures 2–12.

To measure the flux density, we either fitted a Gaussian function with a background linear level if needed, or considered the flux density peak for discrete sources. The rms for each region was estimated by averaging the noise over four boxes surrounding the stellar position, free of sources.

Additionally, we searched for 150-MHz radio emission at the positions of the stars from Tables 1 and 2 using the Tata Institute of Fundamental Research GMRT Sky Survey Alternative Data Release 1 (Intema et al. 2017), and reprocessing of these data (H. Intema, private communication). The rms levels kept in the range 8–10 mJy per beam, except at the position of WR 138a that doubled that value.

One high-mass X-ray binary, WR 145a, and three well-known colliding-wind systems (WR 140, WR 146, and WR 147) were detected. WR 145a is composed by a WN star and a compact

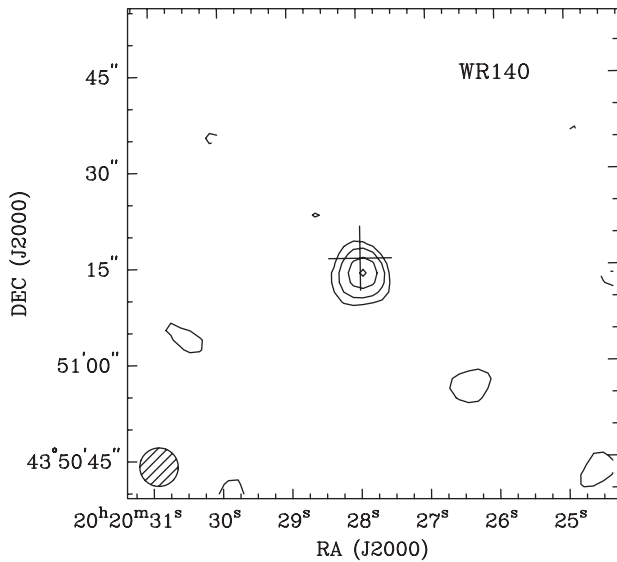


Figure 2. GMRT image of the system WR 140 at 610 MHz. The contour levels are -0.16 , 0.16 ($=2\sigma$), 0.3 , 0.55 , and 0.8 mJy per beam. Hatched, the synthesised beam. Cross hair: optical position of the system (see Table 1).

object, at a distance of 7.4 kpc, and with a period of 0.2 d (Zdziarski et al. 2018), and will not be further analysed here since the nature of the radio emission is out of the scope of this work. The system of WR 140 was detected at 610 MHz, at phase 0.94 of its 7.93-yr period (see Dougherty et al. 2005, and references therein for information about this well-monitored system at other radio frequencies and electromagnetic ranges). The orbital phase corresponding to our observations was derived using the ephemeris of Monnier et al. (2011). WR 146, with a period of many years, hosts a CWR; the latest estimate of its distance is 1.1 kpc. Hales et al. (2017) performed on it a prototype full-polarimetric study that yielded no fractional polarisation of its radio emission above 0.6% (see also references therein). We detected it for the first time at 150 and 610 MHz. The CWB WR 147, according to Rate & Crowther (2020), is located 1.79 kpc from us, a distance three times larger than the former largely accepted value. It follows a long orbit; its radio spectrum was studied by Skinner et al. (1999) and Setia Gunawan et al. (2001). We report its detection at 610 MHz. At 325 MHz, its location, at the border of the FoV, precluded detection below 20 mJy.

Among the O-type stars, Cyg OB2-5 is a system made of at least four components, with probably more than one CWR (see Dzib et al. 2013, and its references). Flux density changes are expected along the orbital phases. Martí et al. (2007) already reported a detection of this system at 610 MHz, with a flux density of 2.41 ± 0.22 mJy, so significantly lower than our measurement of 4.0 ± 0.15 mJy. Regarding the binary Cyg OB2-8A, Blomme et al. (2010) showed that the radio emission is phase locked with the orbital period of 22 d. The radio emission of Cyg OB2-335 was discovered by Setia Gunawan et al. (2003), who proposed it as a CWB, based on observations at 1.4, 4.9, and 8.4 GHz.

5. Discussion

5.1. Detections

Our analysis led to the detection of eleven WR and O-type stars, either at only one or two MHz frequencies. For them, we derived

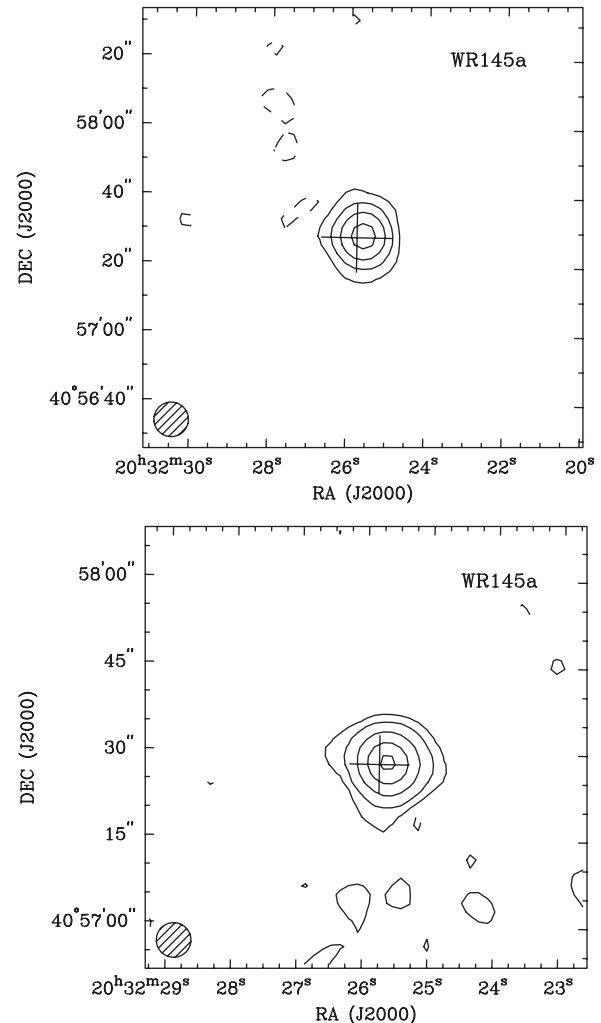


Figure 3. GMRT images of the system WR 145a. Top panel: at 325 MHz; contour levels of -0.8 , 0.8 ($=3\sigma$), 4 , 10 , and 20 mJy per beam. Bottom panel: at 610 MHz; contour levels of -0.3 , 0.3 ($=2\sigma$), 2 , 10 , 30 , and 60 mJy per beam. Hatched, the synthesised beam. Cross hair: optical position of the system (see Table 1).

the spectral indices when possible, and lower limits instead. The main results are summarised in Tables 1 and 2.

5.1.1. The WR systems

The WR sample studied here encompasses nine objects, five of which are known binaries: the four detections reported correspond to that group.

WR 140, the emblematic system of the class of PACWBs, is clearly detected 610 MHz. The upper limit at 325 MHz is consistent with a thermal emission component and an absorbed NT component. Though undetermined, the spectral index appears indeed to be positive.

WR 145a is one of the brightest WR systems in our sample, and this brightness is clearly explained by the physical conditions at work in this system. As a binary system with accreting compact companion, this object does not fit at all in the interpretation scheme of PACWBs at the core of our discussion.

The spectrum of WR 146 at our measurement frequencies appears to be almost flat, suggesting a composite or turned over nature.

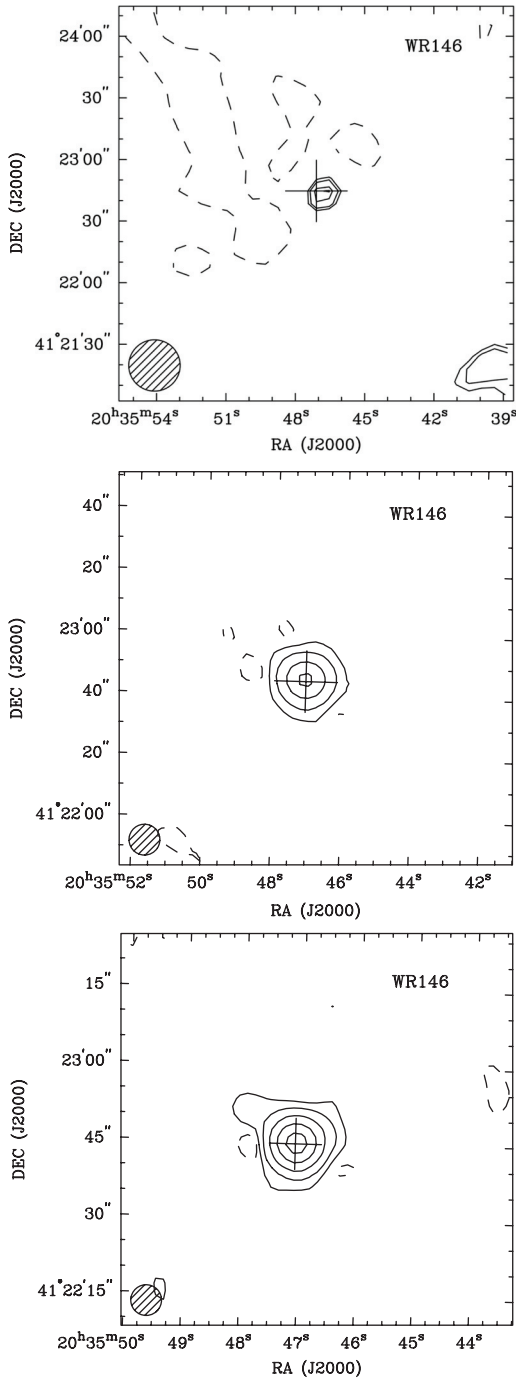


Figure 4. GMRT images of the system WR 146. Top panel: at 150 MHz; contour levels of -18 , 18 ($=3\sigma$), 21 , 27 , and 30 mJy per beam. Central panel: at 325 MHz; contour levels of -1.5 , 1.5 ($=3\sigma$), 10 , 40 , and 90 mJy per beam. Bottom panel: contour levels of -0.75 , 0.75 ($=3\sigma$), 4 , 15 , and 40 mJy per beam. Hatched, the synthesised beam. Cross hair: optical position of the system (see Table 1).

The results on WR 147 offer a similar situation as for WR 140, but with a much higher flux density.

A more detailed discussion of the systems WR 140, WR 146, and WR 147 is developed in Section 5.3.

5.1.2. The detected O-type stars

The O-type stars sample consists of 87 stars or systems, spanning all spectral-type classifications. For many of them, fundamental

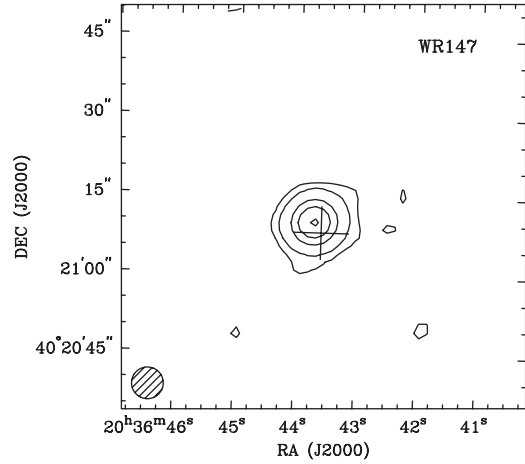


Figure 5. GMRT image of the system WR 147 at 610 MHz. The contour levels are -0.24 , 0.24 ($=3\sigma$), 2 , 5 , 10 , and 18 mJy per beam. Hatched, the synthesised beam. Cross hair: optical position of the system (see Table 1).

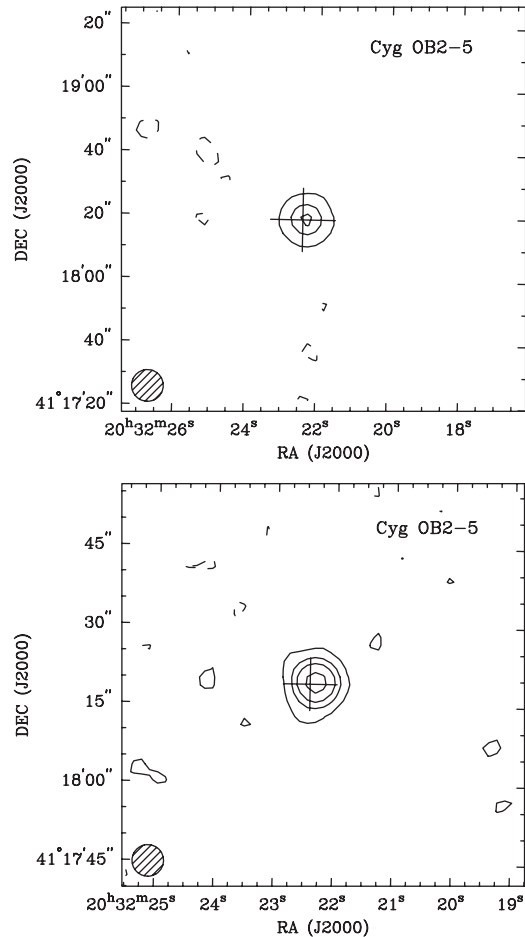


Figure 6. GMRT images of the system Cyg OB2 5. Top panel: at 325 MHz; contour levels of -0.7 , 0.7 ($=3\sigma$), 3 , and 5 mJy per beam. Bottom panel: at 610 MHz; contour levels of -0.15 , 0.17 ($=2\sigma$), 0.75 , 1.5 , and 3 mJy per beam. Hatched, the synthesised beam. Cross hair: optical position of the system (see Table 2).

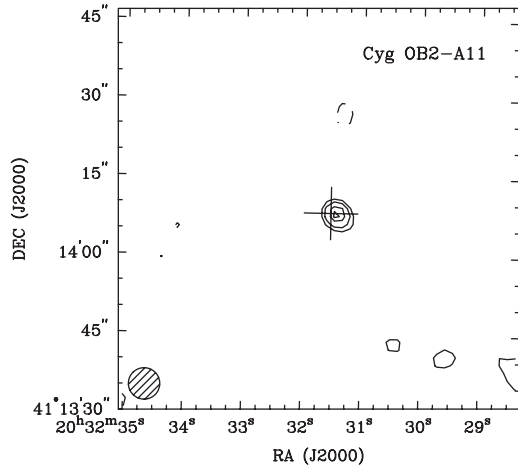


Figure 7. GMRT image of the star Cyg OB2-A11 at 610 MHz. The contour levels are -0.18 , 0.23 ($=3\sigma$), 0.3 , 0.4 , and 0.45 mJy per beam. Hatched, the synthesised beam. Cross hair: optical position of the system (see Table 2).

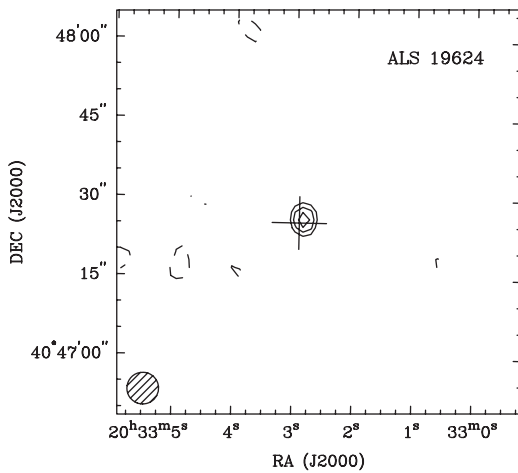


Figure 8. GMRT image of the star ALS 19624 at 610 MHz. The contour levels are -0.25 , 0.25 ($=3\sigma$), 0.35 , and 0.46 mJy per beam. Hatched, the synthesised beam. Cross hair: optical position of the system (see Table 2).

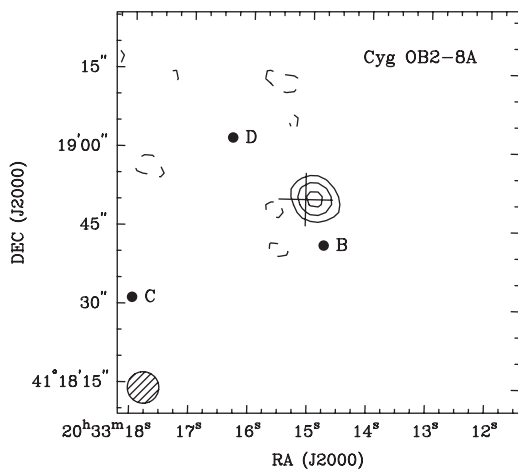


Figure 9. GMRT image of the system Cyg OB2-8A at 610 MHz. The contour levels are -0.35 , 0.30 ($=3\sigma$), 1 , 2 , and 3 mJy per beam. Hatched, the synthesised beam. The cross hair represents the optical position of the 8A system (see Table 2), and the filled circles, those of Cyg OB2-8B, -8C, and -8D stars (see Table A.1).

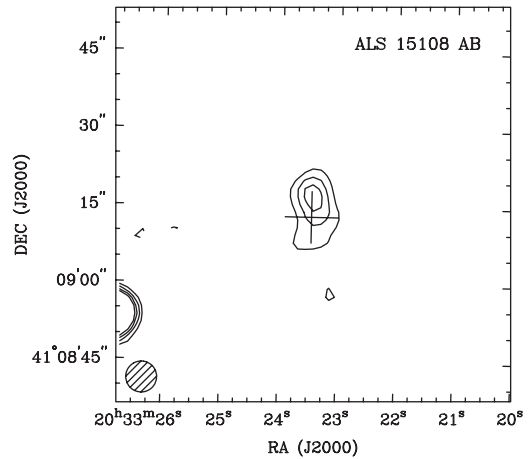
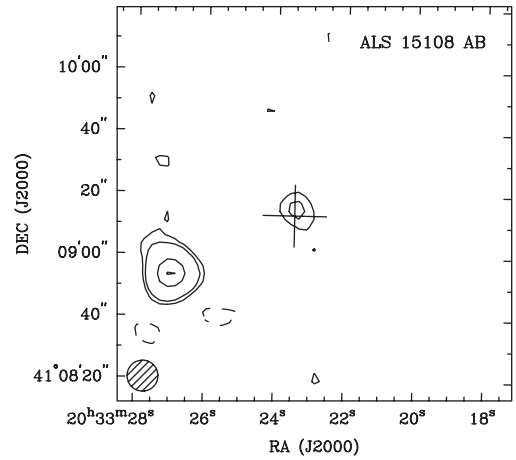


Figure 10. GMRT images of the star ALS 15108 AB. Top panel: at 325 MHz; contour levels of -0.5 , 0.5 ($=3\sigma$), 1 , 5 , and 8 mJy per beam. Bottom panel: at 610 MHz; contour levels of -0.25 , 0.25 ($=3\sigma$), 0.5 , 0.75 , and 1 mJy per beam. Hatched, the synthesised beam. Cross hair: optical position of the system (see Table 2).

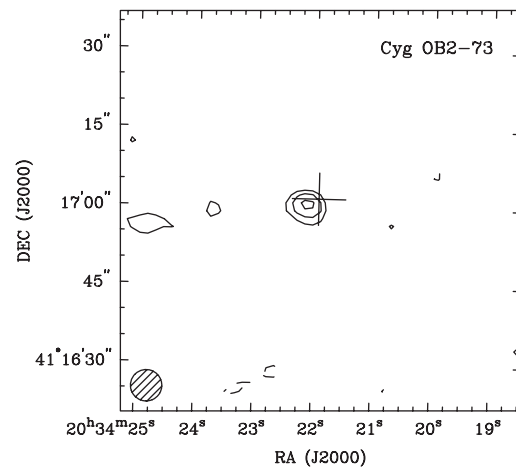


Figure 11. GMRT image of the star Cyg OB2-73 at 610 MHz. The contour levels are -0.22 , 0.22 ($=3\sigma$), 3 and 3.9 mJy per beam. Hatched, the synthesised beam. Cross hair: optical position of the system (see Table 2).

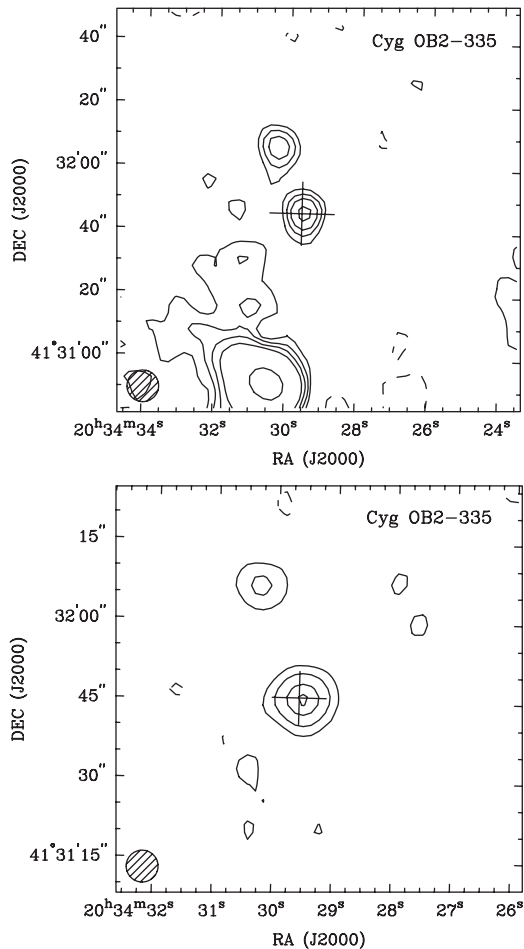


Figure 12. GMRT images of the star Cyg OB2-335. Top panel: at 325 MHz; contour levels of $-0.6, 0.6 (=3\sigma), 1, 1.5, 2.3$ and 10 mJy per beam. Bottom panel: at 610 MHz; contour levels of $-0.2, 0.25 (=3\sigma), 1, 3$ and 5 mJy per beam. Hatched, the synthesised beam. Cross hair: optical position of the system (see Table 2).

parameters such as distance are poorly known and we discuss case by case detections. From the seven detected O-type stars, four are confirmed binary systems, one of which presents a NT spectral index between 325 and 610 MHz, while another displays a positive index. Of the three detected O-type stars catalogued as single, one shows a negative spectral index.

Cyg OB2-5. It is interesting to note that the GMRT measurements clearly confirm the NT nature of the radio emission from this multiple system. If the wind–wind interaction in the 6.7-yr period orbit is at the origin of the synchrotron emission, the stellar separation is large enough to prevent a too severe FFA at these frequencies.

Cyg OB2-A11. Our results do not point to any detection of this binary system at 325 MHz. The loose upper limit at that frequency precludes any reasonable estimate of the spectral index, leading to a large uncertainty on the nature—thermal or NT—of the radio emission.

ALS 19624. Same as Cyg OB2-A11.

Cyg OB2-8A. The upper limit at 325 MHz and the flux density measured at 610 MHz allow to reject a pure optically thin synchrotron emission at these frequencies. The lower emission level at lower frequencies may be explained either by a pure thermal

emission or by a turnover, very likely due to FFA (considering the size of the 22-d orbit and the optical thickness of the winds).

ALS 15108 AB. The negative spectral index reported in Table 2 clearly reveals the NT nature of the source. One can therefore claim the identification of a new member in the catalogue of PACWBs. ALS 15108 AB is likely a binary system with an astrometric companion at an angular distance of $0.7''$ (Mason et al. 2009). Assuming a membership to Cyg OB2 is established, with a distance of about 1.7 kpc, this translates into a separation of the order of 1100 au. Such a stellar separation would indicate a very long orbital period, maybe of the order of centuries. It is not clear whether such a long period system would be able to sustain a wind–wind interaction region capable to significantly accelerate particles. This is especially worth asking given the spectral classification of the star, indicating a rather weak wind in terms of kinetic power. As emphasised by De Becker et al. (2017), the class of PACWBs identified so far is mainly populated by objects with stronger winds, even though the detailed requirements for efficient particle acceleration still deserve to be established. Given the above inferences from the reported separation of the known components of the system, the radio detection presented here can be indicative of a third member of the system, closer to one of the stars.

Cyg OB2-73. Same as Cyg OB2-A11.

Cyg OB2-335. The spectral index quoted in Table 2, between flux density measurements of 325 and 610 MHz, is positive. In the scenario where the synchrotron emission reported on by Setia Gunawan et al. (2003) is produced in a wide orbit, we can complement their results, plotting the radio emission from 325 MHz to 8.4 GHz, and explain a flux density decay at the lower frequencies advocating for the occurrence of an efficient turnover process. A more detailed discussion of this system is developed in Section 5.3.

5.1.3. Comparison with previous results and additional detections

The investigation by Setia Gunawan et al. (2003) allowed the detection of three hot massive systems at 350 MHz, namely, WR 145a, WR 146, and WR 147. They detected them also at 1.4 GHz, together with Cyg OB2-5, Cyg OB2-335, and MWC 349 (a B+B system). The authors also call the attention on other well-known hot massive stars they could not detect (see their Table 9). All of them were included in our targets list, except Cyg OB2-12, another B-type colliding-wind binary system. We proceeded to check for radio emission at the position of those B-type stellar systems in the GMRT images and detected both of them.

Thus, complementary to the analysis on WR and O-type stars, we report on the detection of two B-type systems of CWBs, which were widely studied in the past, though none are part of the PACWB catalogue. Firstly, MWC 349, a B[e]+B0 III $2.4''$ -wide system. Cohen et al. (1985) estimated its distance as 1.2 kpc, according to the spectral type of MWC 349B.^b This system was detected by Tafoya et al. (2004) at 330 MHz with a flux density of 30 ± 10 mJy. We measured the flux densities of 28.6 ± 1.21 mJy (at 325 MHz) and 40.5 ± 0.54 mJy (at 610 MHz) (Figure 13). The value at 325 MHz reported here resulted in eight times lower noise than the Very Large Array measurement. We will analyse the spectrum of MCW 349 in Section 5.3.4.

^bStrelitski et al. (2013) proposed instead MCW 349 as a member of the Cyg OB2 association, if A and B components are unrelated.

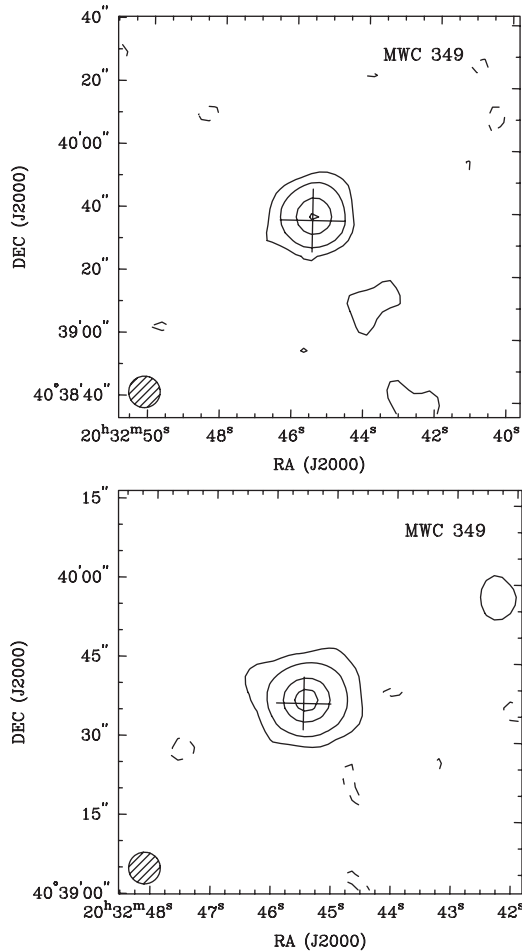


Figure 13. GMRT images of the system MWC 349. Top panel: at 325 MHz; contour levels of -0.7 , 0.9 ($=3\sigma$), 3 , 10 , and 17 mJy per beam. Bottom panel: at 610 MHz; contour levels of -0.3 , 0.3 ($=3\sigma$), 2 , 10 and 20 mJy per beam. Hatched, the synthesised beam. Cross hair: optical position of the system (Zacharias et al. 2012).

The second one, *Cyg OB2-12* (Schulte 12), harbours an evolved B-type hyper-giant. It has been confirmed as a binary system thanks to Fine Guidance Sensor interferometric measurements by Caballero-Nieves et al. (2014), with a stellar separation of about 60 mas, pointing to a likely orbital period of several years. Martí et al. (2007) reported on a detection at 610 MHz with a flux density of 0.93 ± 0.22 mJy. We detected this system at both frequencies (see Figure 14). The peak and integrated flux density values at 610 MHz were 1.35 ± 0.10 and 1.1 ± 0.15 mJy. At 325 MHz, the corresponding values were 1.3 ± 0.20 and 1.9 ± 0.5 mJy, over a higher noise. The error bar on the measurement does not allow to claim any significant variation between both epochs, which would have indicated a likely PACWB status. However, even though the error bars on the flux densities at both frequencies are quite large, we can derive a spectral index $\alpha = -0.87 \pm 0.50$. Such a value, even considering the error bar, cannot be explained by a pure thermal wind emission. In that case, *Cyg OB2-12* fulfils the criteria to be included in the catalogue of PACWBs.

A comparison of the results at 325–350 MHz obtained in Setia Gunawan et al. (2003) and the present work yields the two common detections of WR 145a and WR 146 (WR 147 was at the field border of the GMRT observations). We detected five more stars; for four of them (*Cyg OB2-5*, *-335*, *-12*, and MWC 349) Setia

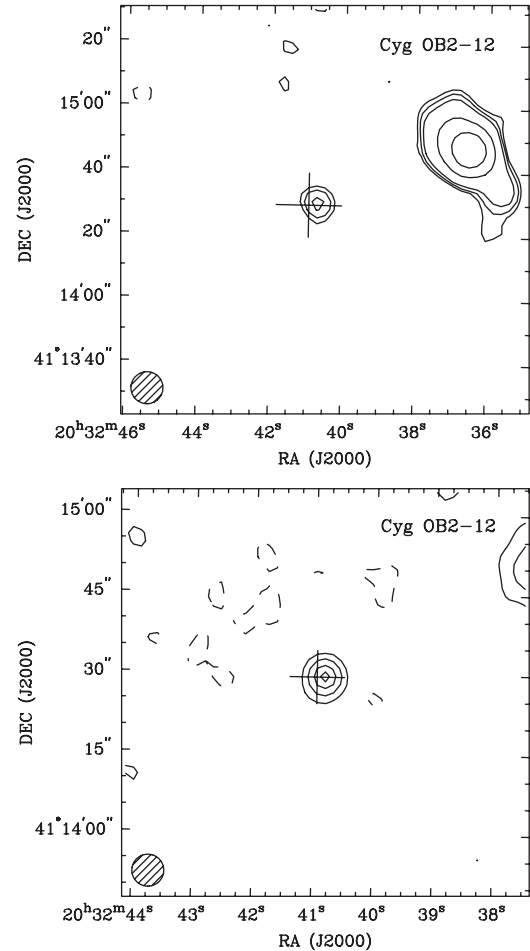


Figure 14. GMRT images of the system *Cyg OB2-12*. Top panel: at 325 MHz; contour levels of -0.5 , 0.7 ($=3\sigma$), 0.9 , 1.2 , 3 , and 6 mJy per beam. Bottom panel: at 610 MHz; contour levels of -0.2 , 0.2 ($=3\sigma$), 0.5 , 0.9 , and 1.2 mJy per beam. Hatched, the synthesised beam. Cross hair: optical position of the system (Gaia Collaboration 2018).

Gunawan et al. (2003) published flux density upper limits. The two sets of flux density measured values/upper limits are in agreement, with the exception of those of WR 146. For this system, the value reported here doubles that from the former study. The observations were performed many years apart (1994.5 vs 2013.9). If the difference is due to orbital phase reasons, this makes WR 146 an unavoidable target to monitor from now on.

5.2. Non detections

WR 138a, *WR 142a*, *WR 142b*, *WR 144*, *WR 145*. Table 3 shows the expected flux densities due to thermal emission from the stellar wind of these WR stars (main component if a system) not detected at centimeter wavelengths, assuming that the stellar mass-loss rate \dot{M} is known. For all cases, the mean molecular weight (μ), the rms ionic charge (Z), and the mean number of electrons per ion (γ) were adopted as 4, 1, and 1, respectively.

These undetected systems are either not known to be binary systems (the first four ones), or a known binary with rather short period (*WR 145*, 22.5 days, Muntean et al. 2009). In the first case, the lack of a CWR prevents the particle acceleration mechanism to operate as expected in shocks produced in wind–wind interaction. This makes any synchrotron emission process unlikely. So only the thermal emission of the (stronger) WR wind should be produced,

Table 3. Expected thermal flux densities at 610 MHz of the WR stars with no previous radio detections. v_∞ : terminal velocity. $T_{\text{eff}} = 0.4 \times T_*$: effective temperature, where T_* is the stellar surface temperature.

Name	$\dot{M} \times 10^5$ ($M_\odot \text{ year}^{-1}$)	v_∞ (km s^{-1})	T_{eff} (kK)	$S_{610\text{MHz}}^{\text{expected}}$ (mJy)
WR 138a	2.0 ⁽¹⁾	700 ⁽¹⁾	16 ⁽¹⁾	0.01
WR 142a	1.9 ⁽²⁾	1700 ⁽³⁾	50 ⁽²⁾	0.08
WR 142b	1.6 ⁽³⁾	1800 ⁽³⁾	28 ⁽³⁾	0.06
WR 144	2.5 ⁽⁴⁾	3500 ⁽⁴⁾	44.8 ⁽⁴⁾	0.05
WR 145	1.6 ⁽⁵⁾	1390 ⁽⁵⁾	20 ⁽³⁾	0.11

References: (1) Gvaramadze et al. (2009); (2) Pasquali et al. (2002); (3) see average parameters per spectral-type classification by Crowther (2007); (4) Sander et al. (2012); (5) Muntean et al. (2009).

but at low frequencies and at such a distance, the flux density falls clearly below the detection threshold of our measurements: see the expected flux density values estimated in Table 3 for WR 138a, WR 142a, and WR 144, compared to the nominal rms value of the 610-MHz mosaic image. In the second case, provided some relativistic electrons are accelerated, it is very likely that FFA would be strong all along the short orbit, considering the optical thickness of the WR winds. Here again, no significant synchrotron emission could be expected at those frequencies on top of the thermal emission from the stellar wind(s) which lies below the detection limit of our measurements. Finally, in the case of WR 138a, tagged as a run-away star, no signs of a bow shock above the noise was detected at any of the observed bands.

Not-detected O-type stars. The O-type stars without radio emission above 3σ ($1\sigma = \text{rms}$) are listed in Table A.1 in the Appendix. One must take into account that the sample, and any trend derived from it, will be biased by the optical and infrared searches performed to discover its stars, due to heavy extinction at those spectral ranges towards the observed region. Besides, the group contains luminosity classes from hyper-giants to dwarfs, thus the origin of their radio emission is expected to be very different.

Having said so, Table A.1 shows that the sample is more populated in late-type ($> O7$) stars than in earlier objects ($< O7$). This is in line with expectations for massive star populations. Such populations result in part from the initial mass function favouring lower mass objects (see, e.g., Zinnecker & Yorke 2007, and references therein). The stellar distributions are also modulated by the evolution time scale, longer for later-type stars. This behaviour should be explained by the flux density-limited nature of the census of stars. Later-type objects are overall fainter, and observational biases lead to significant underestimates of their number.

The lack of detection in general can be interpreted in line with a few basic ideas. If they are not synchrotron radio emitters, the thermal emission from their winds, at a distance of a few kpc, should not be bright enough to be detected at the sensitivity of our measurements. In addition, let us keep in mind that thermal emission is characterised by a positive spectral index, thus much fainter at lower frequencies. Second, an additional radio emission component of synchrotron origin is expected only if these objects are at least binaries. A significant fraction of them should be binaries, but the multiplicity of many of them still needs to be established. Finally, if synchrotron emission is active in some of these objects, FFA is likely to be at work and will be especially efficient in systems with periods not longer than a few weeks. Consequently, the

expected rise of the radio emission at lower frequencies may be compensated by a significant attenuation.

In line with discussions in De Becker et al. (2017), late-type objects are underrepresented in the catalogue of PACWBs. This comes from the lower kinetic power available in weaker wind systems, resulting in less available energy to feed NT processes in the CWR. As a result, their potential weak synchrotron radio emission would lay below the sensitivity limit of our observations. The bulk of the sampled population is thus located in the less favourable part of the stellar parameter space to display hints for particle acceleration. For the few earlier systems, as discussed above, the lack of detection may either be attributed to a single-star status or a significantly free-free absorbed synchrotron emission. We also clarify that a relevant approach would consist in checking for radio detections among actual binaries, in order to address the issue of the fraction of PACWBs among CWBs, as discussed by De Becker et al. (2017). This would require a good knowledge of the multiplicity status of all objects in the field, but this information is poorly determined.

Among the most studied O-type systems in Cyg OB2, there is *Cyg OB2 9* (Schulte 9). This 2.35-yr period system, made of O5–O5.5I and 3–O4III components, is a PACWB whose radio emission at GHz frequencies was investigated in detail by Blomme et al. (2013). It was detected at 610 MHz by Martí et al. (2007) with a flux density of 1.24 ± 0.20 mJy, though not detected in our more recent data. The flux density value at the position of the system, in the 610-MHz images presented here, is 0.2 mJy per beam, at the level of the area rms (we note that diffuse emission is present in the surroundings). This may indicate a variation in the radio emission, indicative of NT emission in line with the criteria proposed by De Becker & Raucq (2013) for synchrotron radiation produced in the CWR.

5.3. On the radio spectra characteristics

Many of the systems under study have been detected at other radio bands, and the measured flux densities reported here allow to complement their spectra. Some of them clearly show a composite spectrum, with thermal and NT contributions.

The radio emission from CWBs is well described by the calculations of Dougherty et al. (2003) and Pittard et al. (2006). The authors produced detailed models of the spectral and spatial distribution using hydrodynamical simulations and solving the radiative transfer equation, and applied them to the systems WR 140 and WR 147. Although those systems were widely observed at radio waves, some parameters, as diverse as inclination or wind clumping factor for instance, remain unknown.

The mentioned models of a CWB take into account thermal (free-free) emission from the individual winds of the hot massive stars that compose the system, and the NT (synchrotron) radiation from the CWR, prone to be modified by thermal absorption along the spectrum. If α_{ff} and α_{NT} are the thermal and synchrotron spectral indices, and τ_0 is the optical depth at 1 MHz (see, for instance, Setia Gunawan et al. 2000), the measured flux density S_ν can be expressed as

$$S_\nu = A \nu^{\alpha_{\text{ff}}} + B \nu^{\alpha_{\text{NT}}} \exp^{-\tau_0 \nu^{-2.1}}, \quad (1)$$

where A and B are constants, and the model assumes that the attenuating ionised medium is external to the population of relativistic electrons that are producing the NT emission.

At low frequencies, the absorption processes of SSA and the RTe (see White & Chen 1995, and references therein) are expected. Williams (1963) showed that for a source size of θ arcsecs in a magnetic field of M Gauss, SSA is critical at the frequency

$$\nu_{\text{SSA}} \approx 2.145 \left(\frac{S_{\nu_{\text{SSA}}}}{\theta^2} \right)^{2/5} M^{1/5} \text{ MHz}, \quad (2)$$

if $S_{\nu_{\text{SSA}}}$ is the maximum flux density in mJy. And the cutoff frequency for RTe (Pacholczyk 1970), if the plasma density is n_e , can be approximated by

$$\nu_{\text{RTe}} = 20 n_e / M \text{ Hz}. \quad (3)$$

In this study, we provide flux density values of various colliding-wind systems, at MHz frequencies. It is not the intention here to dwell into the hydrodynamic models, but performing a phenomenological fit, with illustrative purposes, to exploit the information at very low frequencies and the turnover processes mentioned above: in some way, following the approach of Setia Gunawan et al. (2001). The exercise allows to limit parameters like the NT spectral index and the relevancy of FFA. We discuss individually here the binary systems WR 140, WR 146, WR 147, Cyg OB2-335, and MWC 349. We left aside (i) the multiple system Cyg OB2-5, as complex geometries and system structure, more than one CWR, would increase the degrees of freedom and the putative scenarios to consider, (ii) the 22d-period binary Cyg OB2-8A, since the detection at 610 MHz was obtained by averaging observations one month apart, blurring any indication of the phase-locked emission that was discovered by Blomme et al. (2010), and (iii) Cyg OB2-12, because the measured flux densities presented considerable uncertainty.

The fits were done through a python routine including the function `optimize.curve_fit`, that uses the Levenberg-Marquardt algorithm^c (see also Jones et al. 2001). The routine finds optimal values for the parameters so that the sum of the squared error of the difference (fitted-function value—measured flux density) is minimised. The errors in flux density values are used as weights in the least-squares problem. A caveat here: except for WR 140, we will fit data of different orbital phases, which will most impact on short-period systems.

5.3.1. WR 140

For this system, we considered the flux density values given in Dougherty et al. (2005). The authors observed the object with the very large array at five bands spanning from 1.5 to 22 GHz. Table 4 lists the flux densities corresponding to phase 0.95, and the spectrum is shown in Figure 15. We estimated the separation of the system components on the basis of the orbital solution (Fahed et al. 2011), using the most relevant inclination angle value available now. At the orbital phase of 0.95, the separation is about 1650 R_{\odot} . The position of the stagnation point, where ram pressures of both winds are balanced, is about 75% of the stellar separation away from the WC star ($\sim 1237 R_{\odot}$), and 25% away from the O star ($\sim 413 R_{\odot}$). For the calculations, we assumed wind terminal velocities of 2860 and 3100 km s^{-1} , and mass loss rates of 2×10^{-5} and $2 \times 10^{-6} M_{\odot} \text{ yr}^{-1}$, respectively, for the WC and the O stars (Williams 2011).

Figure 16 is a plot of the estimated radial radio photosphere for a WC7 and a O5.5 star (assuming here a supergiant class), as a function of radio wavelength, based on the free-free emission theory developed by Wright & Barlow (1975). This approach has

Table 4. Radio flux densities of WR systems.

Frequency ν (GHz)	S_{ν} (mJy)	Synth.beam (arcsec ²)	Observing date(s)
WR 140 ^a			
0.61	$0.9 \pm 0.1^{(1)}$	6×6	17/07/2016
1.5	$2.35 \pm 0.7^{(2)}$	46×46	27/09/2000
4.9	$4.74 \pm 0.12^{(2)}$	14×14	27/09/2000
8.4	$6.24 \pm 0.06^{(2)}$	8.2×8.2	27/09/2000
15	$6.94 \pm 0.09^{(2)}$	4.6×4.6	27/09/2000
22	$7.48 \pm 0.14^{(2)}$	3.1×3.1	27/09/2000
WR 146			
0.15	$35 \pm 10^{(1)}$	25×25	2010–2012
0.325	$111 \pm 2^{(1)}$	10×10	06/02/2015
0.61	$121 \pm 4^{(1)}$	6×6	28/11/2014
1.465	$78.4 \pm 0.2^{(3)}$	1.3×1.3	26/10/1996
1.52	$79.8 \pm 1.6^{(4)}$	4.3×4.3	04/05/2015
4.885	$37.6 \pm 1.0^{(3)}$	0.4×0.4	26/10/1996
6.00	$35.7 \pm 0.7^{(4)}$	1×1	04/05/2015
8.435	$29.8 \pm 0.8^{(3)}$	0.24×0.24	26/10/1996
22.46	$17.4 \pm 1.5^{(3)}$	0.1×0.1	26/10/1996
WR 147			
0.325	$16 \pm 4^{(5)}$	55×55	1995
0.61	$20.6 \pm 0.3^{(1)}$	6×6	28/11/2014
1.4	$25.5 \pm 0.5^{(6)(7)}$	12.5×16.3	1989–1997
4.86	$35.4 \pm 0.4^{(7)}$	3.5×5	1988–1997
8.44	$40.3 \pm 4^{(6)}$	1.1×0.8	02/11/1995
14.94	$46.2 \pm 3^{(6)}$	0.7×0.5	02/11/1995
22.46	$52 \pm 5^{(6)}$	0.4×0.3	02/11/1995
42.8	$82.8 \pm 2^{(8)}$	$0.3\text{--}1$	1994–1995

^a In the case of WR 140, the flux densities correspond to phase 0.95. References: 1 = this work; 2 = Dougherty et al. (2005); 3 = Dougherty et al. (2000); 4 = Hales et al. (2017); 5 = Setia Gunawan et al. (2003); 6 = Skinner et al. (1999); 7 = Setia Gunawan et al. (2001); 8 = Contreras et al. (1996). In the case of data from 6, we quote the flux densities derived with IMFIT, but with an error interval to include the TVSTAT values.

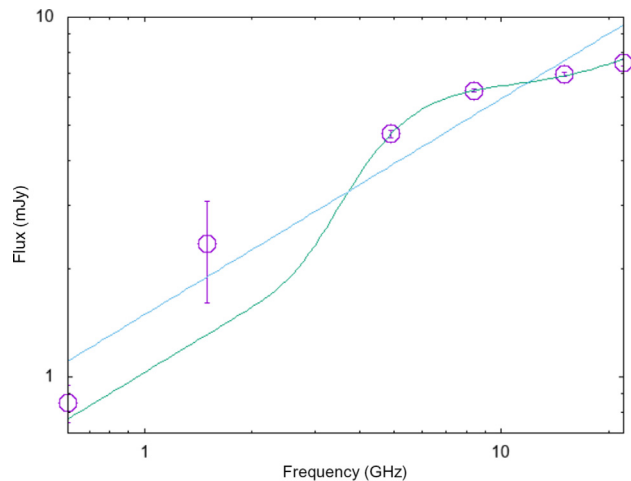


Figure 15. Measured spectrum of WR 140, at orbital phase 0.95 (magenta symbols). The cyan line represents thermal emission ($\alpha_{\text{ff}} = 0.6$). The green one, thermal emission plus NT emission with $\alpha_{\text{NT}} = -0.6$ affected by FFA (see text).

^chttps://docs.scipy.org/doc/scipy/reference/generated/scipy.optimize.curve_fit.html.

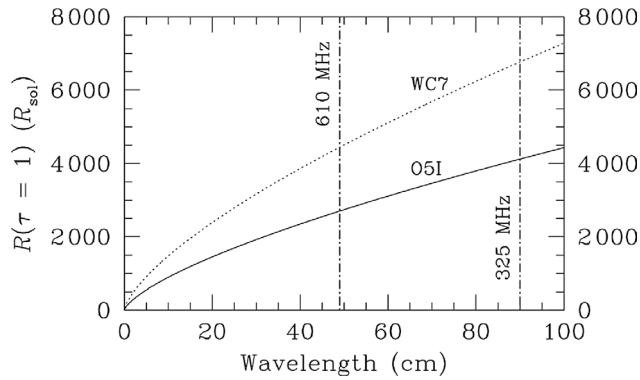


Figure 16. Radio photosphere radius of the two components of WR 140. Vertical lines stand for our two observation wavelengths.

the benefit to provide a quick look at the likelihood that some synchrotron emission would emerge from the stellar winds (see, e.g., De Becker et al. 2019b, for a recent use of this approach). A more accurate quantification of the effect of FFA would need a full radiative transfer treatment along the line of sight at a specific orbital phase, which is out of the scope of this paper. According to Figure 16, the CWR will be inside the radio photospheres at 325-, 610-, and 1500-MHz frequencies of both stars, partially inside the O-star photosphere at 4.9 and 8.64 GHz, and outside the photosphere at 15 and 22 GHz. We will expect then that at lower frequencies, as the CWR is buried by the stellar photospheres, mostly the thermal emission from the winds (dominated by the WC contribution) can reach us; at medium frequencies, the spectrum has thermal contribution from the individual winds, but also NT contribution from the partly unveiled CWR; and at higher frequencies, NT emission from the CWR weakens to be disregarded, remaining the emission from the thermal winds which, besides, increases with frequency.

For WR 140, the fit of Equation (1) with the mentioned routine failed to provide a function that represented the measured flux densities, but parameters with very large uncertainties, even fixing both the thermal and the NT spectral indices. Figure 15 shows the spectrum plotted together with only thermal emission, and with a combination of thermal plus NT emission, this last affected by FFA.

We note that deviations with respect to the simple model of Equation (1) can be argued based on various facts. The actual scenario is much more complex. The spectral index for spherical thermal winds can differ from its canonical value of 0.6 due to wind structure features like clumping, or ionisation; more than one NT emission region can be present, each one with its NT spectral index and normalisation. Besides, the emitting region is extended, and the absorption for each volume element is not the same but depends on the trajectory in the line of sight of the radiation, thus using a constant optical depth is an oversimplification. Finally, uncertainties in absolute calibrations of the flux densities measured with diverse instruments are expected to play a role.

5.3.2. WR 146

To study the radio spectrum of this system, we included our measurements at the GMRT bands of 150, 325, and 610 MHz and the flux densities measured by Dougherty et al. (2000) and by Hales et al. (2017) using the Very Large Array between 1.5 and 22.5 GHz. The 168-mas separation between resolved components of WR 146 measured by Niemela et al. (1998) and the 116-mas separation between the southern thermal source (the WR thermal wind) and

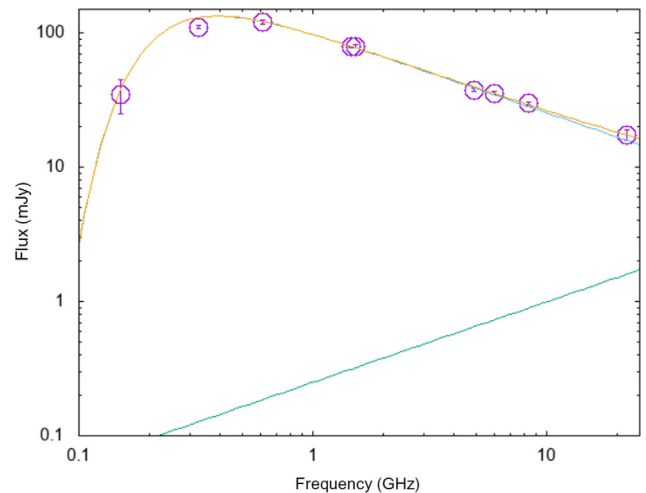


Figure 17. Measured spectrum of WR 146 (magenta symbols): free-free absorption up to 610 MHz (cyan), thermal emission from the WC6 wind (green, $\alpha = 0.6$) and NT emission from the CWR with $\alpha = -0.6$ (orange, see Hales et al. 2017).

the northern NT source (the CWR) reported from MERLIN 5-GHz observations (Dougherty et al. 1996) allowed to derive the distances of the WR and O-type stars to the CWR, $D_{\text{WR-CWR}}$ and $D_{\text{O-CWR}}$.

We detected the system down to 150 MHz ($\lambda = 2$ m). For a WC6 star, the radio photosphere at this frequency is about $10\,000 R_{\odot}$, if we adopt a terminal velocity of 2200 km s^{-1} and a mass loss rate of $1.3 \times 10^{-5} M_{\odot} \text{ yr}^{-1}$. This value is much lower than $D_{\text{WR-CWR}}$ for a system distance of 1.1 kpc ($27\,500 R_{\odot}$). Regarding the primary star, previous works show important uncertainty on the nature of the so-called ‘O-type companion’, which may even be a binary. In such circumstances, it is not possible to make any valid estimate of the photosphere. However, if one stays in the O-type regime with no hidden WR component, one can clearly state that the extension of the photosphere will be significantly smaller than that of the WC star. For this particular system, some spectral features seem to favour a later-type object, which would decrease further its size (especially because of a lower mass loss rate). Then, as $D_{\text{O-CWR}} = \sim 13\,750 R_{\odot}$, the CWR will not be buried in the stellar photospheres, even at the lowest frequency (largest photosphere).

The spectrum of WR 146 presented in Figure 17 shows NT emission, very strong at GHz frequencies. Two different trends can be appreciated: below and above $\nu = 610$ MHz. PACWBs with exposed CWRs are expected to radiate synchrotron emission, with a spectral index α_{NT} related to the electron index p of the relativistic electron (power-law) distribution, such as $\alpha_{\text{NT}} = -(p - 1)/2$. For a strong adiabatic shock in a CWR, Fermi acceleration characterised with $p = 2$ is expected (Bell 1978), thus $\alpha_{\text{NT}} = -0.5$. Hales et al. (2017) observed WR 146 at 1.4 and 6 GHz every 64-MHz sub-bands and found best fits for $\alpha_{\text{NT}} \approx -0.6$. We then adopt for this system, and above 610 MHz, NT emission originated at the CWR $\propto \nu^{-0.6}$. Added to that, we adopt a thermal contribution from the individual winds of the resolved components, considering that it represents 1 mJy at 5 GHz as measured by Dougherty et al. (1996) with $\alpha = 0.6$ (see Figure 17). The fit of the spectrum fixing the spectral indices α_{ff} and α_{NT} of Eq. 1 provided the parameters $A = 0.4 \pm 1.2 \text{ mJy GHz}^{-1}$, $B = 100 \pm 2 \text{ mJy GHz}^{-1}$ and $\tau_0 = 0.05 \pm 0.01$, see Figure 17.

Setia Gunawan et al. (2000) performed a thorough study of this system, from its structure to its energetics. By applying

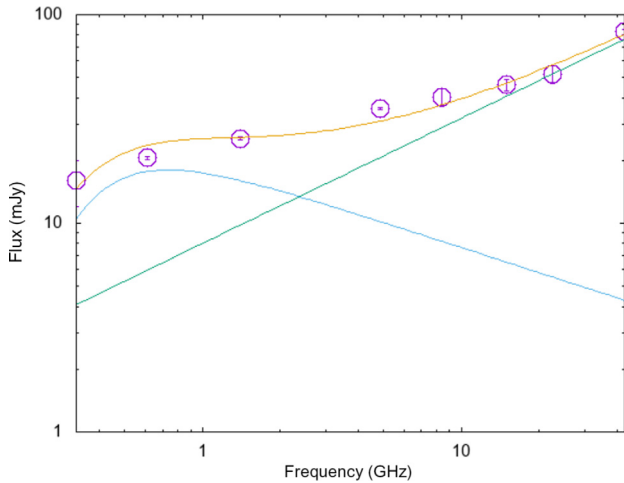


Figure 18. Spectrum of WR 147 (magenta symbols); in orange, the best fit adding thermal emission as $8.8 \nu^{0.6}$ (green) plus NT emission affected by FFA as $21 \nu^{-0.4} \exp(-0.2\nu^{-2.1})$ (cyan).

Equation (2), they conclude that SSA is not relevant and that the turnover is most probably due to FFA. The results of the present fit to the spectrum, which includes the measurement at 150 MHz, explains the turnover in terms of FFA, reinforcing their findings. If this is the case, the results also imply that the RTe, if relevant, will be acting below 150 MHz. The electron density at the CWR derived by Setia Gunawan et al. (2000), scaled to a distance of 1.1 kpc, is $\sim 15 \text{ } 100 \text{ cm}^{-3}$. Following Equation (3), we obtained the lower limit for the magnetic field strength, as $M > 2 \text{ mGauss}$.

5.3.3. WR 147

To analyse the radio spectrum of the WR 147 system, we considered the 610-MHz flux density value reported here, together with those at other bands measured by Setia Gunawan et al. (2001), Skinner et al. (1999), and Contreras et al. (1996). Figure 18 demonstrates that the GMRT flux density value perfectly follows the curves already obtained by the papers cited above, confirming their findings (see Figure 18). We fit a two-term spectrum, with a thermal contribution of $\alpha = 0.6$, and a NT one modified by FFA. The parameters of the fit resulted as $A = 8.8 \pm 1.0 \text{ mJy GHz}^{-1}$, $B = 21 \pm 4 \text{ mJy GHz}^{-1}$, $\alpha_{\text{NT}} = -0.4 \pm 0.25$, $\tau_0 = 0.2 \pm 0.1$, and the curves are shown in Figure 18.

5.3.4. Cyg OB2-335

Figure 19 depicts the radio flux densities measured by Setia Gunawan et al. (2003) and this work. The system has a period of 2.8 d (Kobulnicky et al. 2014), which makes very difficult to reconcile the negative spectral index quoted between measurements at 1.4 and 4.9 GHz by Setia Gunawan et al. (2003), since synchrotron radiation could hardly escape from being absorbed by the optically thick thermal winds of the binary components. De Becker et al. (2017) proposed to investigate the object in searching for a potential third component of the system in a wider orbit, capable of developing an unveiled CWR. In such a case, and if the third orbit is large enough for the measurements given in Table 4 (along 1996 to 2014) to be comparable, then we can fit the spectrum using Equation (1). Due to the low number of points, and the large errors for some of them, the fitting routine provided parameters without the covariance matrix. The resulting expression was $S_\nu =$

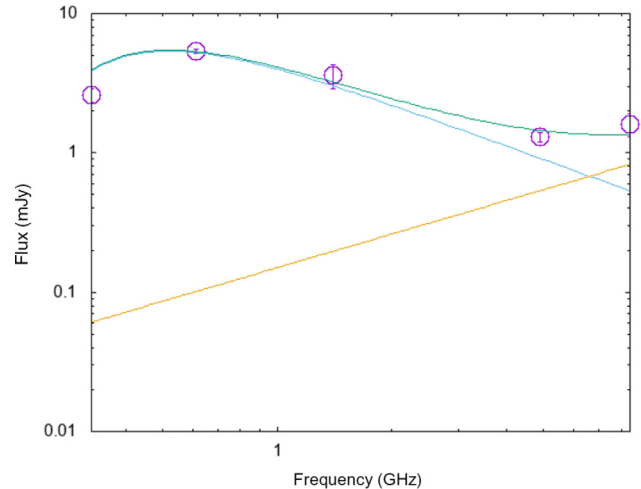


Figure 19. Measured spectrum of Cyg OB2-335 (magenta symbols); in green, the best fit adding thermal emission as $0.14 \nu^{0.7}$ (orange) plus NT emission affected by FFA as $4.5 \nu^{-0.95} \exp(-0.13\nu^{-2.1})$ (cyan).

$0.14 \nu^{0.7} + 4.5 \nu^{-0.95} \exp(-0.13\nu^{-2.1})$. Figure 19 shows the problems in fitting the flux density at 325 MHz, taking into account just FFA. Alternatively, let us explore the idea that the turnover is due to SSA. We do not have any direct information on the size of the emitting region (θ in Equation (2)). One can just say that, as some synchrotron radiation is detected, the source should be significantly located out of the radio photosphere. This does not tell us about its exact size, but its extension may be of the same order. We thus determined the size of the radio photosphere of the O7 V component of the system. For typical mass loss rate and terminal velocity values of $2.4 \times 10^{-7} \text{ M}_\odot \text{ yr}^{-1}$ and 2500 km s^{-1} (Vink, de Koter, & Lamers 2000), we get $\theta \sim 1000 \text{ R}_\odot$. In the framework of these assumptions, if SSA is in action, the magnetic field strength is of the order of 1 mGauss. If the assumed size is 5 times smaller, the magnetic field strength is $3 \mu\text{Gauss}$. Even though such values are compatible with expectations from a CWR, we caution that their determination relies on strong assumptions. In particular, there is not warranty that SSA is active and the emission region size is still undetermined.

5.3.5. MWC 349

The B[e] star MCW 349A has been largely studied by means of radio observations at many bands, at first due to its high brightness. Cohen et al. (1985) discovered a bipolar emitting region or wind at 15 MHz of ‘hourglass’ shape, and a kind of bridge at 5 GHz that separates it from its proposed companion, MWC 349B. Tafuya et al. (2004) presented observations taken with the very large array at 330 MHz up to 44.34 GHz, from which they measured the corresponding flux densities. Using data from 1.425 to 44.34 GHz, the authors calculated the spectral index of the ionised wind as 0.64 ± 0.03 and proposed that the ionised emission came from the photoevaporation of a disk in the equatorial plane of the star. According to the investigation of Rodriguez et al. (2007), the former shape of the bipolar outflow has been changing to an almost square shape.

We complemented the flux densities from 1.4 to 44 GHz given by Tafuya et al. (2004) with the ones obtained here, and a 2.7 GHz flux density value given by Hjellming et al. (1973) (see Table 5). The set allowed us to fit a thermal contribution to the spectrum

Table 5. Radio flux densities of OB+OB systems.

Frequency ν (GHz)	S_ν (mJy)	Synth.beam (arcsec ²)	Observing date(s)
OB2-335			
0.325	$2.6 \pm 0.3^{(1)}$	10×10	04/11/2013
0.61	$5.4 \pm 0.2^{(1)}$	6×6	29/11/2014
1.4	$3.6 \pm 0.7^{(2)}$	13×13	1996-1997
4.886	$1.3 \pm 0.1^{(2)}$	not prov.	25/02/2001
8.44	$1.6 \pm 0.3^{(2)}$	not prov.	25/02/2001
MWC 349			
0.325	$28.6 \pm 1.21^{(1)}$	10×10	04/11/2013
0.61	$40.5 \pm 0.54^{(1)}$	6×6	29/11/2014
1.425	$76.4 \pm 6.4^{(3)}$	1.3×1.2	05/12/1996
2.695	$100 \pm 15^{(4)}$	3×3	1972-1973
4.85	$154.8 \pm 8.5^{(3)}$	0.4×0.4	05/12/1996
8.31	$183.5 \pm 9.5^{(3)}$	0.2×0.2	31/12/1988
14.94	$380.0 \pm 21.2^{(3)}$	0.1×0.1	05/12/1996
22.367	$446.2 \pm 44.8^{(3)}$	0.09×0.08	29/03/1990
43.34	$635.0 \pm 95.6^{(3)}$	0.04×0.03	16/12/1996

not prov.: not provided by authors. References: (1) this work; (2) Setia Gunawan et al. (2003); (3) Tafoya et al. (2004); (4) Hjellming et al. (1973).

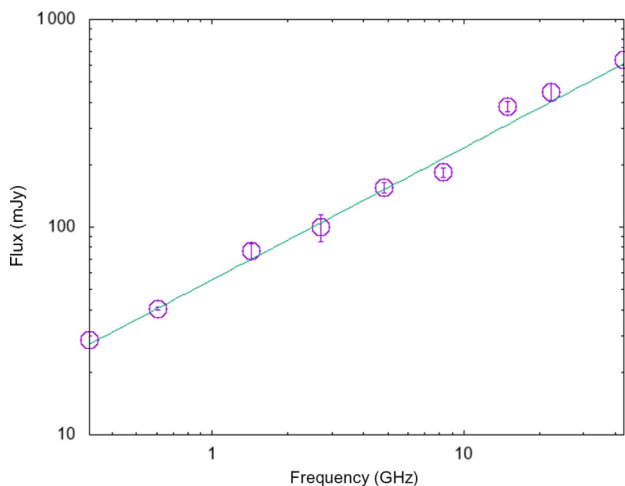


Figure 20. Measured spectrum of MWC 349 (magenta symbols); in green, the best fit considering thermal emission as $55.7 \nu^{0.64}$.

in the form of $S_\nu = A \nu^{\alpha_{ff}}$, with $A = 55.71 \pm 1.21 \text{ mJy GHz}^{-1}$ and $\alpha_{ff} = 0.636 \pm 0.021$, confirming the previous result. In Fig. 20, we displayed the observed flux densities and the fit function.

6. Conclusions

We reported on the investigation of a 15-square degrees survey of the Cygnus region using the GMRT, at 325-MHz and 610-MHz frequencies. Our main objective was to investigate the low-frequency radio emission from the population of massive stars in that region, with emphasis on O-type and WR stars, along with a couple of B-type remarkable objects.

1. Our investigation allowed us to provide evidence that massive stars, and in particular colliding-wind binary systems,

are able to emit radio continuum down to 150 MHz. Out of nine WR objects in the field, we detected four of them at least at one frequency. For O-type stars, we detected seven objects out of 87 present in the field of our survey. We interpret the low detection rate for O-type stars in terms of (i) thermal emission much fainter at low frequencies, (ii) strong FFA by the stellar winds that is strongly attenuating any putative synchrotron emission (for binary systems), and (iii) low NT energy budget in a population dominated by later-type objects characterised by a lower wind kinetic power.

2. The measurements at these frequencies appear also to be especially appropriate to investigate synchrotron emission from CWBs. Our data enabled us to identify two new members in the class of PACWBs, namely ALS 15108 AB and Cyg OB2-12. With these two additional members, the total number of known PACWBs amounts to about 45 objects so far.
3. We also focused on the WR systems WR 140, WR 146, and WR 147 to discuss their main spectral properties, making use of broadband radio measurements including our new measurements and previous ones obtained at higher frequencies. In general, the spectral shape can be well interpreted in terms of free-free absorbed synchrotron emission at lower frequencies, on top of a thermal emission from the stellar winds. In this context, the extension of the radio photosphere and the geometry of the system plays a key role. WR 146, the only system with flux density measurements down to 150 MHz, presents a clear turnover. These results may indicate that the RTe does not seem to be relevant at the frequencies investigated.
4. For the O+O system Cyg OB2-335, other processes than FFA have to be invoked to match the observations, but the current information on this system precludes further analysis. Dedicated, simultaneous observations, at the highest angular resolution and sensitivity are crucial to disentangle the processes at work in this system, and search for the evidence of a third companion.
5. Finally, the high signal-to-noise flux density measurements at MHz frequencies provided here for the B+B system MWC 349 confirm the thermal nature of its emitting wind.

Acknowledgements. The authors are grateful to the referee, whose comments and suggestions resulted in improving the analysis and presentation of the article. The radio data presented here were obtained with the GMRT. The GMRT is operated by the National Centre for Radio Astrophysics of the Tata Institute of Fundamental Research. We thank the staff of the GMRT that made these observations possible. P.B. acknowledges support from ANPCyT PICT 0773-2017, M.E. Colazo for computing assistance, S. del Palacio for fruitful discussions and the staff at NCRA, Pune, for a wonderful stay. This research has made use of the SIMBAD database, operated at Strasburg astronomical Data Center (CDS), France, and of NASA's Astrophysics Data System bibliographic services.

References

- Abdo, A. A., et al. 2010, *ApJ*, **723**, 649
 Bell, A. R. 1978, *MNRAS*, **182**, 147
 Benaglia, P., del Palacio, S., Ishwara-Chandra, C. H., De Becker, M., Isequilla, N. L., & Saponara, J. 2019, *A&A*, **625**, A99

- Benaglia, P., Ishwara-Chandra, C. H., Intema, H., Colazo, M. E., & Gaikwad, M. 2020, submitted
- Benaglia, P., Marcote, B., Moldón, J., Nelan, E., De Becker, M., Dougherty, S. M., & Koribalski, B. S. 2015, *A&A*, **579**, A99
- Blomme, R., De Becker, M., Runacres, M. C., van Loo, S., & Setia Gunawan, D. Y. A. 2007, *A&A*, **464**, 701
- Blomme, R., De Becker, M., Volpi, D., & Rauw, G. 2010, *A&A*, **519**, A111
- Blomme, R., Nazé, Y., Volpi, D., De Becker, M., Prinja, R. K., Pittard, J. M., Parkin, E. R., & Absil, O. 2013, *A&A*, **550**, A90
- Caballero-Nieves, S. M., et al. 2014, *AJ*, **147**, 40
- Callingham, J. R., Tuthill, P. G., Pope, B. J. S., Williams, P. M., Crowther, P. A., Edwards, M., Norris, B., & Kedziora-Chudczer, L. 2019, *NatAs*, **3**, 82
- Cohen, M., Biegging, J. H., Dreher, J. W., & Welch, W. J. 1985, *ApJ*, **292**, 249
- Comerón, F., & Pasquali, A. 2012, *A&A*, **543**, A101
- Contreras, M. E., Rodríguez, L. F., Gomez, Y., & Velazquez, A. 1996, *ApJ*, **469**, 329
- Crowther, P. A. 2007, *ARA&A*, **45**, 177
- Cutri, R. M., et al. 2003, VizieR Online Data Catalog, **II/246**
- De Becker, M., Benaglia, P., Romero, G. E., & Peri, C. S. 2017, *A&A*, **600**, A47
- De Becker, M., Ishwara-Chandra, C. H., & Benaglia, P. 2019a, Bulletin de la Société Royale des Sciences de Liège, **88**, 262
- De Becker, M., Isequilla, N. L., & Benaglia, P. 2019b, *A&A*, **623**, A163
- De Becker, M., & Raucq, F. 2013, *A&A*, **558**, A28
- Del Palacio, S., Bosch-Ramon, V., Romero, G. E., & Benaglia, P. 2016, *A&A*, **591**, A139
- Dougherty, S. M., Beasley, A. J., Claussen, M. J., Zauderer, B. A., & Bolingbroke, N. J. 2005, *ApJ*, **623**, 447
- Drury, L. O. 1983, *RPPH*, **46**, 973
- Dougherty, S. M., Pittard, J. M., Kasian, L., Coker, R. F., Williams, P. M., & Lloyd, H. M. 2003, *A&A*, **409**, 217
- Dougherty, S. M., & Williams, P. M. 2000, *MNRAS*, **319**, 1005
- Dougherty, S. M., Williams, P. M., & Pollacco, D. L. 2000, *MNRAS*, **316**, 143
- Dougherty, S. M., Williams, P. M., van der Hucht, K. A., Bode, M. F., & Davis, R. J. 1996, *MNRAS*, **280**, 963
- Dzib, S. A., Rodríguez, L. F., Loinard, L., Mioduszewski, A. J., Ortiz-León, G. N., & Araud, A. T. 2013, *ApJ*, **763**, 139
- Eichler, D., & Usov, V. 1993, *ApJ*, **402**, 271
- Fahed, R., et al. 2011, *MNRAS*, **418**, 2
- Gaia Collaboration 2018, VizieR Online Data Catalog, **I/345**
- Gvaramadze, V. V., et al. 2009, *MNRAS*, **400**, 524
- Gvaramadze, V. V., Miroshnichenko, A. S., Castro, N., Langer, N., & Zharikov, S. V. 2014, *MNRAS*, **437**, 2761
- Hales, C. A., Benaglia, P., del Palacio, S., Romero, G. E., & Koribalski, B. S. 2017, *A&A*, **598**, A42
- Hjellming, R. M., Blankenship, L. C., & Balick, B. 1973, *Nature Physical Science, Nature Physical Science*, **242**, 84
- Hoag, A. A., & Applequist, N. L. 1965, *ApJS*, **12**, 215
- Intema, H. T. 2014, SPAM: Source Peeling and Atmospheric Modeling, Astrophysics Source Code Library (ascl:1408.006)
- Intema, H. T., Jagannathan, P., Mooley, K. P., & Frail, D. A. 2017, *A&A*, **598**, A78
- Jones, E., et al. 2001, SciPy: Open source scientific tools for Python, <http://www.scipy.org/>
- Kennedy, M., Dougherty, S. M., Fink, A., & Williams, P. M. 2010, *ApJ*, **709**, 632
- Kiminki, D. C., et al. 2007, *ApJ*, **664**, 1102
- Knödseder, J. 2000, *A&A*, **360**, 539
- Kobulnicky, H. A., Gilbert, I. J., & Kiminki D. C. 2010, *ApJ*, **710**, 549
- Kobulnicky, H. A., et al. 2014, *ApJS*, **213**, 34
- Koljonen, K. I. I., & Maccarone, T. J. 2017, *MNRAS*, **472**, 2181
- Lépine, S., Wallace, D., Shara, M. M., Moffat, A. F. J., Niemela, & V. S. 2001, *AJ*, **122**, 3407
- Littlefield, C., Garnavich, P., Marion, G. H. H., Vinkó, J., McClelland, C., Rettig, T., & Wheeler, J. C. 2012, *AJ*, **143**, 136
- Mahy, L., Rauw, G., De Becker, M., Eenens, P., & Flores, C. A. 2013, *A&A*, **550**, A27
- Maíz Apellániz, J., et al. 2016, *ApJS*, **224**, 4
- Maíz Apellániz, J., et al. 2019, *A&A*, **626**, A20
- Martí-Devesa, G., Reimer, O., Li, J., & Torres, D. F. 2020, *A&A*, **635**, A141
- Martí, J., Paredes, J. M., Ishwara Chandra, C. H., & Bosch-Ramon, V. 2007, *A&A*, **472**, 557
- Mason, B. D., Hartkopf, W. L., Gies, D. R., Henry, T. J., & Helsel, J. W. 2009, *AJ*, **137**, 3358
- Monnier, J. D., et al. 2011, *ApJ*, **742**, L1
- Muntean, V., Moffat, A. F. J., Chené, A. N., & de La Chevrotière, A. 2009, *MNRAS*, **399**, 1977
- Niemela, V. S., Shara, M. M., Wallace, D. J., Zurek, D. R., & Moffat, A. F. J. 1998, *AJ*, **115**, 2047
- Pacholczyk, A. G. 1970, Radio astrophysics. Nonthermal processes in galactic and extragalactic sources
- Paredes, J. M., Martí, J., Ishwara-Chandra, C. H., & Bosch-Ramon, V. 2007, *ApJ*, **654**, L135
- Pasquali, A., Comerón, F., Gredel, R., Torra, J., & Figueras, F. 2002, *A&A*, **396**, 533
- Pittard, J. M., Dougherty, S. M., Coker, R. F., O'Connor, E., & Bolingbroke, N. J. 2006, *A&A*, **446**, 1001
- Pshirkov, M. S. 2016, *MNRAS*, **457**, L99
- Rate, G., & Crowther, P. A. 2020, *MNRAS*, **493**, 1512
- Reipurth, B., & Schneider, N. 2008, Star Formation and Young Clusters in Cygnus. ASP, 36
- Reitberger, K., Kissmann, R., Reimer, A., Reimer, O., & Dubus, G. 2014a, *ApJ*, **782**, 96
- Reitberger, K., Kissmann, R., Reimer, A., & Reimer, O. 2014b, *ApJ*, **789**, 87
- Reitberger, K., Kissmann, R., Reimer, A., & Reimer, O. 2017, *ApJ*, **847**, 40
- Reitberger, K., Reimer, A., Reimer, O., & Takahashi, H. 2015, *A&A*, **577**, A100
- Rodríguez, L. F., Gómez, Y., & Tafuya, D. 2007, *ApJ*, **663**, 1083
- Sanchez-Bermudez, J., et al. 2019, *A&A*, **624**, A55
- Sander, A., Hamann, W. R., & Todt, H. 2012, *A&A*, **540**, A144
- Setia Gunawan, D. Y. A., de Bruyn, A. G., van der Hucht, K. A., & Williams, P. M. 2000, *A&A*, **356**, 676
- Setia Gunawan, D. Y. A., de Bruyn, A. G., van der Hucht, K. A., & Williams, P. M. 2003, *ApJS*, **149**, 123
- Setia Gunawan, D. Y. A., van der Hucht, K. A., Williams, P. M., Henrichs, H. F., Kaper, L., Stickland, D. J., & Wamsteker, W. 2001, *A&A*, **376**, 460
- Simón-Díaz, S., & Herrero, A. 2007, *A&A*, **468**, 1063
- Skinner, S. L., Itoh, M., Nagase, F., & Zhekov, S. A. 1999, *ApJ*, **524**, 394
- Sota, A., Maíz Apellániz, J., Walborn, N. R., Alfaro, E. J., Barbá, R. H., Morrell, N. I., Gamen, R. C., & Arias, J. I. 2011, *ApJS*, **193**, 24
- Strelitskiy, V., Biegging, J. H., Hora, J., Smith, H. A., Armstrong, P., Lagergren, K., & Walker, G. 2013, *ApJ*, **777**, 89
- Tafuya, D., Gómez, Y., & Rodríguez, L. F. 2004, *ApJ*, **610**, 827
- Tavani, M., et al. 2009, *ApJ*, **698**, L142
- Uyaniker, B., Fürst, E., Reich, W., Aschenbach, B., & Wielebinski, R. 2001, *A&A*, **371**, 675
- Vink, J. S., de Koter, A., & Lamers, H. J. G. L. M. 2000, *A&A*, **362**, 295
- White, R. L., & Becker, R. H. 1995, *ApJ*, **451**, 352
- White, R. L., & Chen, W. 1995, in IAU Symposium, ed. K. A. van der Hucht, & P. M. Williams, Wolf-Rayet Stars: Binaries; Colliding Winds; Evolution (Vol. 163), 438
- Williams, P. J. S. 1963, *Nature*, **200**, 56
- Williams, P. 2011, Bulletin de la Société Royale des Sciences de Liège, **80**, 595
- Williams, P. M., Dougherty, S. M., Davis, R. J., van der Hucht, K. A., Bode, M. F., & Setia Gunawan, D. Y. A. 1997, *MNRAS*, **289**, 10
- Wright, A. E., & Barlow, M. J. 1975, *MNRAS*, **170**, 41
- Zacharias, N., Finch, C. T., Girard, T. M., Henden, A., Bartlett, J. L., Monet, D. G., & Zacharias, M. I. 2012, VizieR Online Data Catalog, **I/322A**
- Zdziarski, A. A., et al. 2018, *MNRAS*, **479**, 4399
- Zinnecker, H., & Yorke, H. W. 2007, *ARA&A*, **45**, 481

A. Non-detected O-type stars

Here, we present [Table A.1](#), with the undetected O stars: star name, spectral-type classification and its reference, and coordinates. The rms was estimated using the image at 610 MHz, over an area of $\sim 4' \times 4'$, computed over four boxes around the star.

Table A.1. Non-detected O-type stars in the area of the Cygnus region observed in the present study.

Name	Spectral type classification	Reference	RA, Dec (J2000) [h,m,s],[d,',"]	rms at 610 MHz (mJy per beam)
HD 193117	O9.5II	(1)	20:16:59.89,+40:50:37.4	0.10
LS III+41 14	O9.5V(n)	(2)	20:17:05.52,+41:57:46.9	0.10
HD 228759	O6.5V(n)((f))z	(2)	20:17:07.54,+41:57:26.5	0.10
HD 193322AaAb	O9IV(n)+B1.5V	(2)	20:18:06.99,+40:43:55.5	0.15
TYC 3159-6-1	O9.5-O9.7Ib	(3)	20:18:40.34,+41:32:45.1	0.10
J20190610+4037004	O9.7Iab	(4)	20:19:06.10,+40:37:00.4	0.30
J20194916+4052090	O9.5V	(4)	20:19:49.15,+40:52:08.9	0.25
ALS 11244	O4.5III(n)(fc)p	(2)	20:22:37.78,+41:40:29.2	0.10
HD 229196	O6II(f)	(2)	20:23:10.79,+40:52:29.9	0.15
ALS 19302	O9.5:V	(5)	20:23:14.55,+40:45:19.1	0.20
HD 229202	O7.5V(n)((f))	(2)	20:23:22.84,+40:09:22.5	0.80
ALS 11321	O9III	(4)	20:25:06.52,+40:35:49.8	0.20
J20272428+4115458	O9.5V	(4)	20:27:24.28,+41:15:45.8	0.10
BD+40 4179	O8Vz	(2)	20:27:43.62,+40:35:43.5	0.15
J20283039+4105290	OC9.7Ia	(4)	20:28:30.39,+41:05:29.1	0.12
ALS 11376	O7	(4)	20:28:32.03,+40:49:02.9	0.40
ALS 11378	O8.5V	(4)	20:28:40.81,+43:08:58.5	0.10
J20293480+4120089	O9.5V	(4)	20:29:34.80,+41:20:08.9	0.15
CPR2002-A18	O8V	(4)	20:30:07.88,+41:23:50.4	0.10
J20301839+4053466	O9V	(4)	20:30:18.39,+40:53:46.6	0.20
Cyg OB2-B17	O6Iaf+O9:Ia:	(2)	20:30:27.30,+41:13:25.3	0.15
HD 195592	O9.7Ia	(6)	20:30:34.97,+44:18:54.9	0.15
ALS 15129	O6.5V	(4)	20:30:39.80,+41:36:50.7	0.10
CPR2002-A26	O9V	(4)	20:30:57.72,+41:09:57.5	0.10
ALS 19637	O7V((f))	(4)	20:31:00.20,+40:49:49.7	0.10
Cyg OB2-1	O8IV(n((f))	(2)	20:31:10.54,+41:31:53.5	0.10
ALS 15133	O9.5IV	(2)	20:31:18.33,+41:21:21.7	0.10
ALS 21081	O7Ib(f)	(4)	20:31:36.91,+40:59:09.0	0.10
Cyg OB2-3A	O8.5Ib(f)+O6III:	(2)	20:31:37.51,+41:13:21.0	0.15
ALS 15116	O8V	(4)	20:31:45.40,+41:18:26.7	0.10
Cyg OB2-20	O9.7IV	(2)	20:31:49.67,+41 28:26.5	0.10
GOS G080.03+00.94 01	O7.5Vz	(2)	20:31:59.61,+41:14:50.5	0.10
Cyg OB2-4A	O7III((f))	(2)	20:32:13.83,+41:27:12.0	0.10
Cyg OB2-14	O9V	(7)	20:32:16.56,+41:25:35.7	0.10
RLP 145	O9.5V	(8)	20:32:19.75,+41:44:46.9	0.15
Cyg OB2-15	O8III	(2)	20:32:27.67,+41:26 22.1	0.10
ALS 19628	O9.5IV	(4)	20:32:30.31,+40:34:33.2	0.10
CPR2002-A38	O8V	(2)	20:32:34.87,+40:56:17.3	0.12
CPR2002-A25	O8III	(2)	20:32:38.44,+40:40:44.5	0.12
Cyg OB2-16	O07.5IIV(n)	(2)	20:32:38.56,+41:25:13.8	0.11
Cyg OB2-6	O8.5V(n)	(2)	20:32:45.45,+41:25:37.5	0.10
Cyg OB2-17	O8V	(2)	20:32:50.01,+41:23:44.7	0.10
ALS 15111	O8V	(2)	20:32:59.19,+41:24:25.5	0.10
Cyg OB2-41	O9.7III(n)	(2)	20:32:59.64,+41:15:14.7	0.12
ALS 15131	O7.5V((f))	(2)	20:33:02.92,+41:17:43.1	0.13

Table A.1. (continued).

Name	Spectral type classification	Reference	RA, Dec (J2000) [h,m,s],[d,',"]	rms at 610 MHz (mJy per beam)
Cyg OB2-22A	O3If*	(2)	20:33:08.76,+41:13:18.6	0.10
Cyg OB2-22B	O6V((f))	(2)	20:33:08.84,+41:13:17.4	0.10
Cyg OB2-22C	O9.5III n	(2)	20:33:09.60,+41:13:00.5	0.10
Cyg OB2-50	O9.5III n	(6)	20:33:09.60,+41:13:00.6	0.10
Cyg OB2-22D	O9.5Vn	(2)	20:33:10.12,+41:13:10.1	0.10
Cyg OB2-9	O4.5If	(2)	20:33:10.73,+41:15:08.2	0.12
ALS 15148	O6.5-V	(2)	20:33:13.27,+41:13:28.7	0.10
ALS 15128	O8V	(4)	20:33:13.69,+41:13:05.8	0.10
Cyg OB2-7	O3If*	(2)	20:33:14.12,+41:20:21.9	0.11
Cyg OB2-8B	O6II(f)	(2)	20:33:14.76,+41:18:41.8	0.11
Cyg OB2-23	O9V	(7)	20:33:15.71,+41:20:17.2	0.11
Cyg OB2-8D	O8.5V(n)	(2)	20:33:16.33,+41:19:02.0	0.11
Cyg OB2-24	O8V(n)	(2)	20:33:17.48,+41:17:09.3	0.14
Cyg OB2-8C	O4.5(fc)p var	(2)	20:33:17.98,+41:18:31.2	0.14
ALS 15115	O8V	(2)	20:33:18.05,+41:21:36.9	0.12
ALS 15123	O9V	(4)	20:33:21.02,+41:17:40.1	0.14
Cyg OB2-25 A	O8.5Vz	(2)	20:33:25.54,+41:33:27.0	0.10
ALS 15134	O8.5Vz	(2)	20:33:26.75,+41:10:59.5	0.10
Cyg OB2-74	O8V	(4)	20:33:30.32,+41:35:57.9	0.10
Cyg OB2-70	O9.5IV(n)	(2)	20:33:37.00,+41:16:11.3	0.12
ALS 15124	O7V	(4)	20:33:40.86,+41:30:18.9	0.10
Cyg OB2-10	O9.7Iab	(2)	20:33:46.11,+41:33:01.1	0.11
J20335842+4019411	O9:	(4)	20:33:58.42,+40:19:41.2	0.14
Cyg OB2-27AB	O9.7V(n)+O9.7V:(n)	(2)	20:33:59.53,+41:17:35.5	0.12
ALS 15145	O8.5V	(4)	20:34:04.86,+41:05:12.9	0.14
Cyg OB2-11	O5.5Ifc	(2)	20:34:08.51,+41:36:59.4	0.10
Cyg OB2-75	O9V	(2)	20:34:09.52,+41:34:13.7	0.10
Cyg OB2-29	O7.5V(n)((f))z	(2)	20:34:13.51,+41:35:03.0	0.10
J20341605+4102196	O9.5V	(4)	20:34:16.05,+41:02:19.6	0.11
J20342894+4156171	O9V	(4)	20:34:28.94,+41:56:17.0	0.10
Cyg OB2-A24	O6.5III(f)	(2)	20:34:44.11,+40:51:58.5	0.16
CPR2002-A10	O9V	(9)	20:34:55.11,+40:34:44.3	0.30
ALS 19627	O9.7Iab	(4)	20:34:56.06,+40:38:17.9	0.15
MASSI J2035238+412203	O8.5V	(10)	20:35:23.79,+41:22:03.7	0.15
ALS 19631	O5V((f))	(2)	20:36:04.50,+40:56:13.0	0.25

References: (1): Mahy et al. (2013); (2): Galactic O-star catalogue v. 4.2 (<http://gosc.cab.inta-csic.es/gosc.php>); (3): Gvaramadze et al. (2014); (4): Comerón & Pasquali (2012); (5): Hoag & Applequist (1965); (6): Sota et al. (2011); (7): Kiminki et al. (2007); (8): Simón-D az & Herrero (2007); (9): Kobulnicky et al. (2010); (10): Cutri et al. (2003).